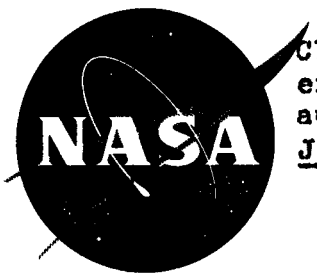

TECHNICAL MEMORANDUM

X-268

INVESTIGATION OF THE ROLLING STABILITY DERIVATIVES OF TWO HYPERSONIC GLIDERS OF PARABOLIC PLAN FORM AT HIGH SUBSONIC SPEEDS

By Donald D. Arabian

Langley Research Center
Langley Field, Va.

NATIONAL AERONAUTICS AND SPACE ADMINISTRATION
WASHINGTON
April 1960

NATIONAL AERONAUTICS AND SPACE ADMINISTRATION

TECHNICAL MEMORANDUM X-268

INVESTIGATION OF THE ROLLING STABILITY DERIVATIVES OF TWO HYPERSONIC GLIDERS OF PARABOLIC PLAN FORM AT HIGH SUBSONIC SPEEDS*

By Donald D. Arabian

SUMMARY

An experimental investigation was conducted to determine the characteristics of the stability derivatives, damping in roll and yawing moment due to rolling velocity about the stability axes, of two hypersonic glider models of aspect ratio 0.62 and 1.25. The models were parabolic in plan form with flat undersurfaces and semielliptical cross sections. The results for a range of Mach numbers from 0.4 to 0.9 with angles of attack up to about 15° and roll rate up to 37 radians per second indicated linear characteristics of the basic force and moment data. The effect of model geometry on the derivatives was appreciable and the trends with angle of attack and Mach number are shown. The contribution of a vertical tail on the aspect-ratio-0.62 model is indicated.

INTRODUCTION

A variety of aerodynamic shapes has been proposed for hypersonic glider vehicles. Of these, one group which lack wings as such has thick body sections and blunt rear sections. The question arises as to the nature of the dynamic stability of these thick wingless shapes flying within the atmosphere since certain stability requirements must be satisfied whether inherent to the shape or artifically supplied.

An experimental investigation was therefore conducted in the Langley 16-foot transonic tunnel to determine the nature of two of the derivatives, rolling moment due to rolling velocity and yawing moment due to rolling velocity, for two glider models of aspect ratio 0.62 and 1.25. The shapes of the models were parabolic in plan form with flat

*Title, Unclassified.

undersurfaces and semielliptical cross sections. These models are identical to two of a family of shapes for which the static aerodynamic characteristics were previously investigated (ref. 1) and are similar to those for which static aerodynamic characteristics are presented in reference 2.

Results of the investigation are presented in this paper for a range of angle of attack, Mach number, and roll rate. The effect of aspect ratio on the derivatives is indicated in comparison plots, and the effect of a vertical fin is shown for one configuration.

SYMBOLS

The basic data are presented with respect to the body axes while the stability derivatives are presented with respect to the stability axes system. The origin of the axis system was at the center of gravity of the models at which point the moments were evaluated. The center of gravity of each model was located at the respective centroid of the plan view.

A	plan-form aspect ratio
b	body span, ft
h	distance of vertical-tail centroid above the longitudinal body axis, in.
l	distance from center of gravity to the vertical-tail centroid measured along the longitudinal body axis, in.
M	free-stream Mach number
p	rolling velocity, radians/sec
q	dynamic pressure, lb/sq ft
R	Reynolds number, based on body span
S	plan-form area, sq ft
V	free-stream velocity, ft/sec
x	model longitudinal station measured from nose, in.
z	model vertical distance from undersurface, in.
$\frac{pb}{2V}$	tip helix angle, radians

α true angle of attack measured from the model bottom to free stream, deg

α_0 nominal angle of attack, deg

σ sidewash angle, radians

C_N normal-force coefficient, $\frac{\text{Normal force}}{qS}$

C_l rolling-moment coefficient, $\frac{\text{Rolling moment}}{qSb}$

C_n yawing-moment coefficient, $\frac{\text{Yawing moment}}{qSb}$

C_Y side-force coefficient, $\frac{\text{Side force}}{qS}$

$$C_{l_p} = \frac{\partial C_l}{\partial \frac{pb}{2V}}$$

$$C_{n_p} = \frac{\partial C_n}{\partial \frac{pb}{2V}}$$

MODEL AND APPARATUS

Three-view sketches of the two models are shown in figures 1(a) and 1(b). Both models had parabolic plan forms, flat bottom surfaces, and semielliptical sections normal to the stream. The model with an aspect ratio of 0.62 is called the narrow configuration while the model with an aspect ratio of 1.25 is called the wide configuration. The narrow model was also tested with a vertical fin which was 5.5 percent of the body-plan-form area.

The models were constructed of fiber glass, a foam plastic, and resin. The center of gravity was closely alined with the electrical center of the balance by lead shot glued within the model at appropriate points.

The models were supported at about the center of gravity through a 5-component balance which was attached to a sting extending from the

rear end of the model. Steady rolling velocity was supplied by rotating the entire sting support system by means of a variable-speed electric motor which was mounted in the test section on a strut as shown in figure 2. Photographs of the models on the stability apparatus in the tunnel are shown in figure 3.

Four stings were available to set the model at the specific values of angle of attack: 0°, 5°, 10°, or 15°. The offsets in the stings were such that the axis of rotation passed through the center of gravity of the model. A counterweight on an arm supplied balance for the sting offsets.

Tests and Corrections

The tests were made in the Langley 16-foot transonic tunnel. Typical distributions of the Mach number along the center line of the tunnel are presented in figure 4 with the test apparatus in the test section. The test Mach number was taken as the local free-stream Mach number in the tunnel at the model center-of-gravity station. The tunnel speed was adjusted to give the desired test Mach numbers of 0.4, 0.6, 0.8, and 0.9. The angle of attack was varied from 0° to about 15° and roll rates from 15.7 to 37.7 radians per second. The corresponding average Reynolds number and helix angle range encountered for the test Mach number range are shown in figure 5 for both models.

The balance data were corrected for inertia forces and for moments arising from the fact that the model center of gravity, the electrical center of the balance, and the axis of rotation did not exactly coincide. The inertia corrections were obtained by enclosing the model with a container and rotating the entire system for the range of test conditions. (See fig. 2.) In this manner the aerodynamic forces and moments were eliminated. No corrections were made for any interference effects. However, a check was made to determine the interference of the counterweight system of the stings. A brief test without the counterweight system showed these interference effects to be negligible.

RESULTS

Force and Moment Data

The variation with helix angle of the coefficients of rolling moment, yawing moment, and side force with respect to body axes are presented for the wide model in figure 6, for the narrow model in figure 7, and for the narrow model with a vertical tail in figure 8. The trends shown by the variation of the coefficients with helix angle

for these three configurations were generally similar for the range of variable investigated. The variations with helix angle of the values of rolling- and yawing-moment coefficient were generally linear in all cases, the data showing very consistent trends and little scatter. The data for side-force coefficient, however, are in general erratic to the extent that definite trends are not well defined. Most of the scatter in the side-force data are due to low sensitivity of the side-force element of the strain-gage balance. Under some test conditions this balance is required to withstand large values of side force and was designed accordingly; the relatively small values of side force encountered in these tests required only a small fraction of the balance side-force capacity, and scatter in the data represents limits of balance accuracy at small loads. To illustrate, note in the figures for either model that the moment data tend to zero as the helix angle tends to zero. On the other hand, the side-force data for constant Mach numbers, in general, do not tend to zero. But if the data for all the Mach numbers are averaged, this average tends to zero.

Stability Derivatives

The stability derivatives C_{l_p} and C_{n_p} were obtained by dividing the basic moment data by $pb/2V$ and transferring these values to the stability axis system. The results are presented in figures 9, 10, and 11 where the variation of the derivatives with angle of attack is shown for a range of Mach numbers and roll rate. A specific symbol is used for each value of the roll rate but curves are faired for only the maximum and minimum roll rates tested. Damping in roll for the wide model is shown in figure 9 to decrease with angle of attack up to about 5°. At the higher angles of attack, C_{l_p} generally increased. The yaw due to rolling velocity about the stability axes increased in the negative direction up to an angle of attack of about 10° and then decreased with increasing angle. Essentially, the roll rate had little effect on C_{n_p}.

The damping in roll for the narrow model in figure 10 increased about threefold as the angle of attack was increased from 0° to about 15°. Yaw due to rolling velocity for this model varied similar to that of the wide model for the lower Mach numbers. The largest magnitudes of C_{n_p} occurred at lower angles of attack with increasing roll rate. For Mach numbers of 0.80 and 0.90, C_{n_p} increased or remained fairly constant above an angle of attack of 10° depending on the rate of roll. A more direct indication of Mach number effects is shown in figure 12, where the derivatives for the narrow model with and without a tail and the wide model are plotted against Mach number. Results are presented

for the angle-of-attack range for the lowest roll rate tested. The wide-model derivatives were little affected by Mach number up to a Mach number of about 0.80.

For the narrow model with or without a tail, the large variations with Mach number of the derivative at high angles of attack are possibly accentuated by Reynolds number effects. At the lower angles the effects of Mach number were similar to those of the wide model.

Comparison of Model Configurations

A comparison of the variations of C_{l_p} and C_{n_p} with angle of attack is shown in figure 13 for the wide and narrow models for Mach numbers of 0.4 and 0.9. The solid and dashed curves represent the wide and narrow models, respectively. The difference in the data for the two models at low angles of attack may be considered to be mainly due to a change in aspect ratio. At an angle of attack of 0°, doubling the aspect ratio (0.62 to 1.25) about doubled the damping in roll. But the rate of increase of damping with angle of attack was greater for the narrow model such that at an angle of attack of about 15° the damping for the narrow model was greater than that for the wide model. This general trend was exhibited at all values of Mach number and roll rates investigated. The trends of these results may be explained by considering the flow fields of the two models. The difference in the two flow fields arises from the comparatively large differences in the streamwise sections, that is, the side views of the two models shown in figure 1. The relatively thin leading-edge sections in the forebody together with the high leading-edge sweep angle of the narrow model would be expected to create leading-edge separation which would roll up into concentrated vortices in the flow field above the upper surface. The flow field of the wide model, on the other hand, may be expected to be free of concentrated vortices for the angles of attack of these tests due to the relatively blunt leading edges and the lower leading-edge sweep angles of the sections. Although local separation may occur at the lower leading-edge discontinuity, reattachment would be expected because of the thick section. The probable existence of separation of the flow and concentrated vortices for the narrow model and attached flow for the wide model can be supported by force data with the aid of the analysis of reference 3. It has been shown in reference 3 that concentrated vortices caused by leading-edge separation for highly swept leading-edge wings can appreciably increase the lift over that given by Jones' slender-wing theory. Slender-wing theory indicates the slope of the normal-force curve to be essentially constant with angle of attack and proportional to the aspect ratio. If there is separation of the flow at the leading edge which results in concentrated vortices above the surface, a term is added to the slender-wing theory according

to reference 3 to account for the influence of the vortices on the wing loading. Consequently, the slope of the normal-force curve increases with increasing angle of attack. Figure 14 presents the average of the normal-force coefficient data for a number of roll rates at various angles of attack for both models at Mach numbers of 0.4 and 0.9. Note the normal-force curve for the wide model has a constant slope whereas that of the narrow model increases with increasing angle of attack.

Therefore, the narrow model is affected by concentrated vortices since the normal-force curve slope increases with angle of attack and the wide model has essentially attached flow on the upper surface since its normal-force curve slope is constant with angle of attack. Furthermore, the lift-curve slopes of figure 14 for the two models at the low angles of attack differ approximately by a factor of two, which is in agreement with slender-body theory. Since C_{l_p} is proportional to the normal-force curve slope, trends of the damping in roll may be predicted if the normal-force curve slopes are known. Therefore, figure 14 indicates the following trends which are in agreement with figure 13. At an angle of attack of 0°, the narrow model (aspect ratio 0.62) would be expected to have half as much damping in roll as the wide model (aspect ratio 1.25). With increasing angle of attack, C_{l_p} of the narrow model should be greater than that of the wide model since the normal-force curve slope of the narrow model becomes greater than that of the wide model at the higher angles of attack. Figure 13 also shows that model differences had little effect on C_{n_p} except at high angles of attack at the higher values of Mach numbers. Here C_{n_p} increased in the negative direction for the narrow model.

Effect of a Vertical Tail

The contribution of a vertical tail to the stability derivatives C_{l_p} and C_{n_p} was investigated on the narrow model for the purpose of indicating the effect of a tail on a thick low-aspect-ratio shape. The basic data of the investigation are presented in figure 11. The variations with angle of attack of the increment of C_{l_p} and C_{n_p} due to the vertical tail are presented in figures 15 and 16, respectively, for a high and low roll rate. Included in the figures is a plot of the estimated contribution of the tail by the method of reference 4 for incompressible flow to C_{n_p} and C_{l_p}. The equation of reference 4 for estimating the contributions may be written as

$$\Delta C_{l_p} = \left(C_{Y_\beta}\right)_t \left[\frac{l}{b}(h \cos \alpha - l \sin \alpha)\right]\left[-\frac{2}{b}(h \cos \alpha - l \sin \alpha) + \frac{\partial \sigma}{\partial \frac{pb}{2V}}\right]$$

and

$$\Delta C_{n_p} = -\left(C_{Y_\beta}\right)_t \left[\frac{l}{b}(l \cos \alpha + h \sin \alpha)\right]\left[-\frac{2}{b}(h \cos \alpha - l \sin \alpha) + \frac{\partial \sigma}{\partial \frac{pb}{2V}}\right]$$

where the tail contribution of side force due to sideslip $\left(C_{Y_\beta}\right)_t$ was obtained from experimental data. The contribution of the sidewash due to the rolling wing $\frac{\partial \sigma}{\partial \frac{pb}{2V}}$ was approximated by extrapolation of existing sidewash calculations to the model aspect ratio and tail location for these tests. Furthermore, the sidewash was assumed to be constant with angle of attack.

The calculated values of ΔC_{l_p} were small for all Mach numbers and angles of attack of the test. Experimental values of ΔC_{l_p} were small except at high angles of attack, in which case the damping contribution of the tail became appreciable. It should be noted that the calculated values do not include the effect of the tail on the body. These effects would appear mainly as a contribution to rolling moment.

The calculated variations of C_{n_p} due to the tail with angle of attack were in fair agreement with the measured variations. There is, however, a constant shift of the calculated ΔC_{n_p} curve which may be attributed to the error of approximating the sidewash. The results of figure 16 show the tail contribution to C_{n_p} to increase in the negative direction with increasing angle of attack.

CONCLUSIONS

An investigation of two parabolic plan-form bodies of aspect ratio 1.25 and 0.62 to evaluate damping in roll and yawing moment due

to rolling about the stability axes at Mach numbers from 0.4 to 0.9 for a range of roll rates up to 37 radians per second and angles of attack up to 15° has indicated the following:

1. For both models the variations of the rolling- and yawing-moment coefficients with respect to the body axes were linear with roll rate.

2. The effect of aspect ratio on the derivatives with respect to the stability axes was appreciable. At low angles of attack the higher aspect ratio model had higher damping in roll. However, at the high angles of attack the effect of leading-edge separation increased the damping in roll for the low-aspect-ratio model over that for the high-aspect-ratio model. At low angles of attack for all Mach numbers tested the difference in yawing moment due to rolling for both models was small. At higher Mach numbers and angles of attack the yawing moment due to rolling velocity increased in the negative direction for the low-aspect-ratio model.

3. The effects of a vertical tail on the low-aspect-ratio model were small except at high angles of attack. The tail contribution to yawing moment due to rolling increased appreciably with increasing angle of attack.

Langley Research Center,
National Aeronautics and Space Administration,
Langley Field, Va., December 16, 1959.

REFERENCES

1. Queijo, Manuel J.: Static Stability Characteristics of Three Thick Wing Models With Parabolic Plan Form at a Mach Number of 3.11. NASA TM X-141, 1959.

2. Lange, Roy H.: Exploratory Investigation at a Mach Number of 5.20 of the Longitudinal Aerodynamic Characteristics of Flat-Bottom Bodies. NACA RM L56E30, 1956.

3. Brown, Clinton E., and Michael, William H., Jr.: On Slender Delta Wings With Leading-Edge Separation. NACA TN 3430, 1955.

4. Michael, William H., Jr.: Analysis of the Effects of Wing Interference on the Tail Contributions to the Rolling Derivatives. NACA Rep. 1086, 1952. (Supersedes NACA TN 2332.)

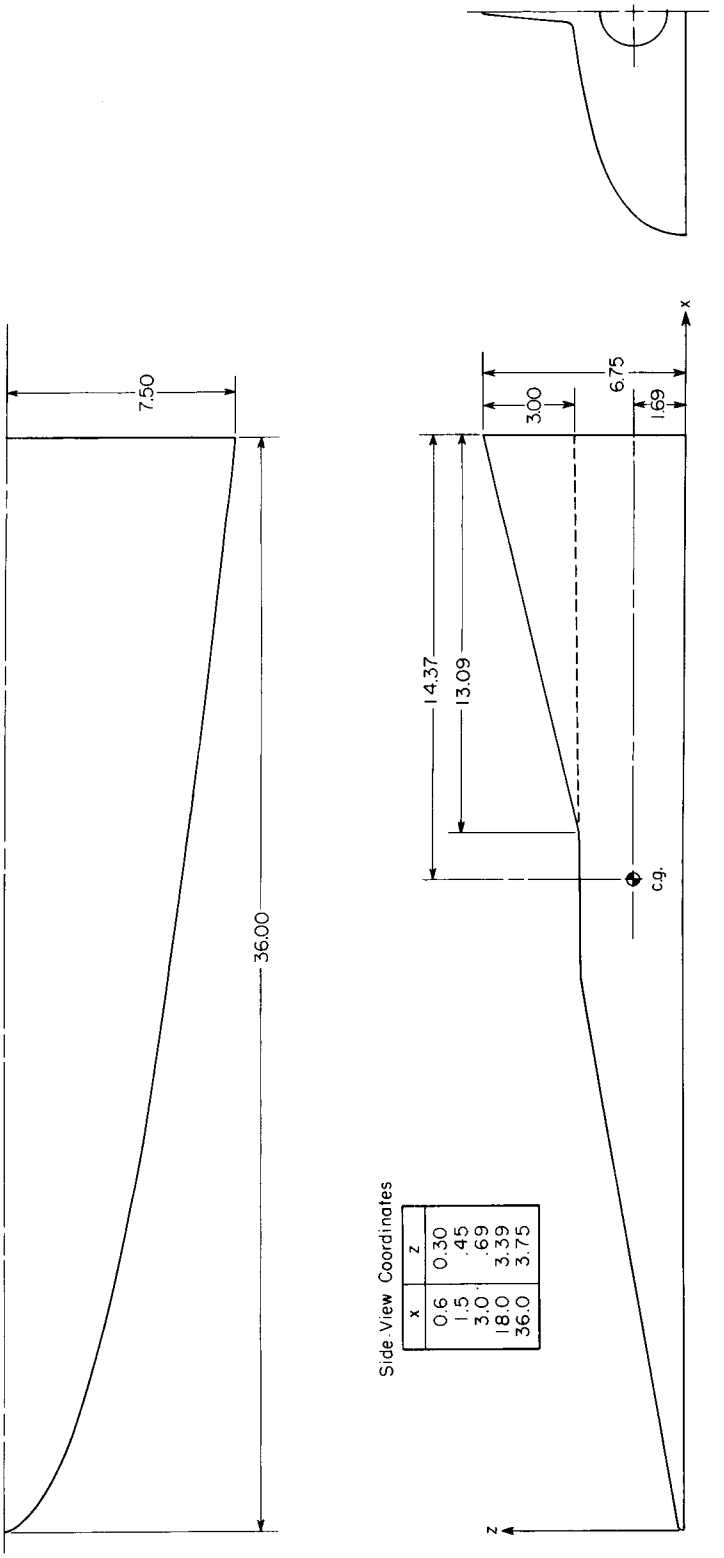

(a) Aspect-ratio-0.62 model.

Figure 1.- General arrangement of models. All dimensions are in inches.

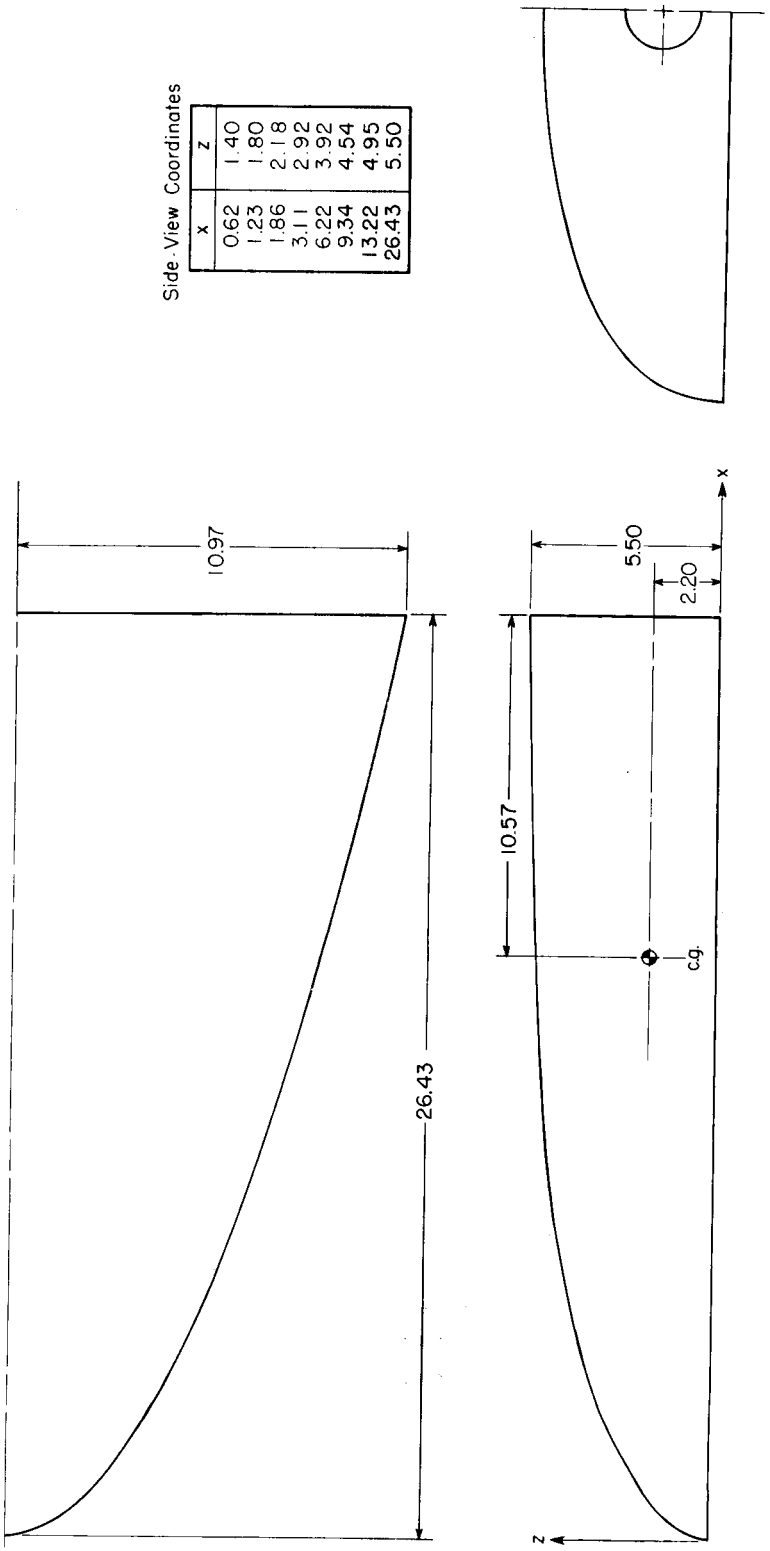

(b) Aspect-ratio-1.25 model.

Figure 1.- Concluded.

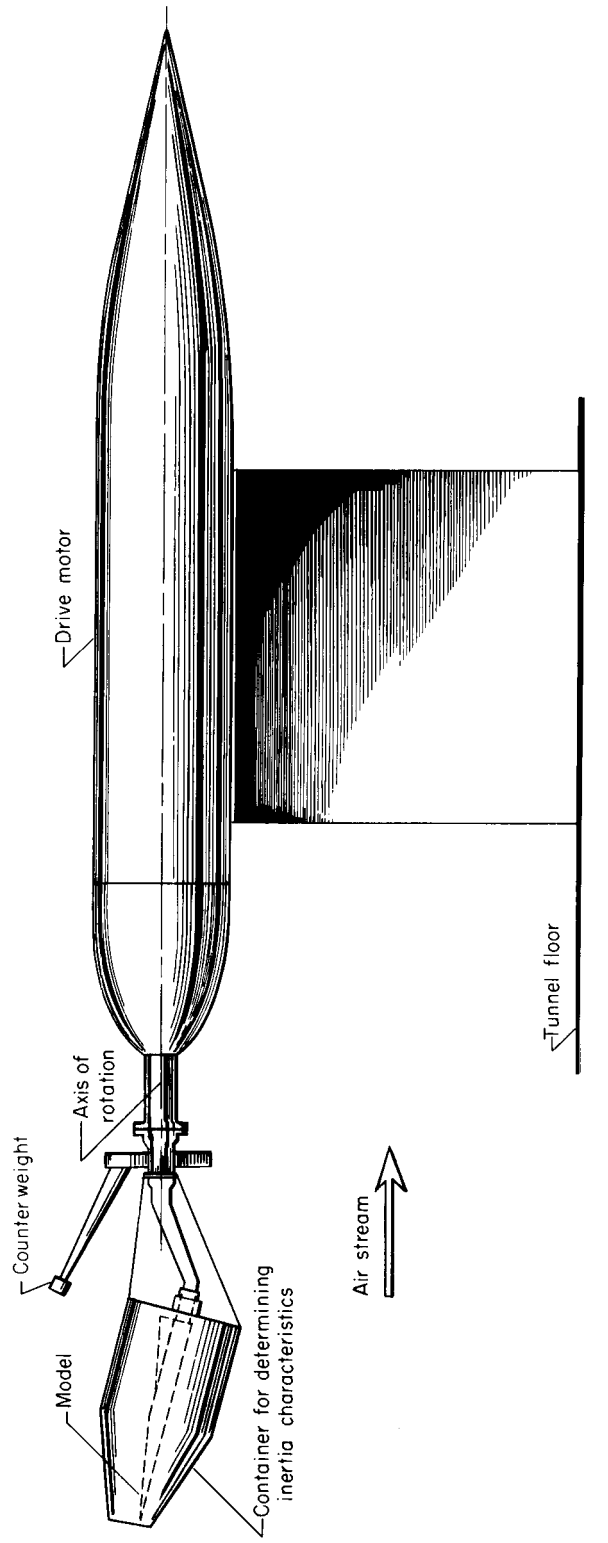

Figure 2.- Sketch of the Langley 16-foot transonic tunnel test apparatus.

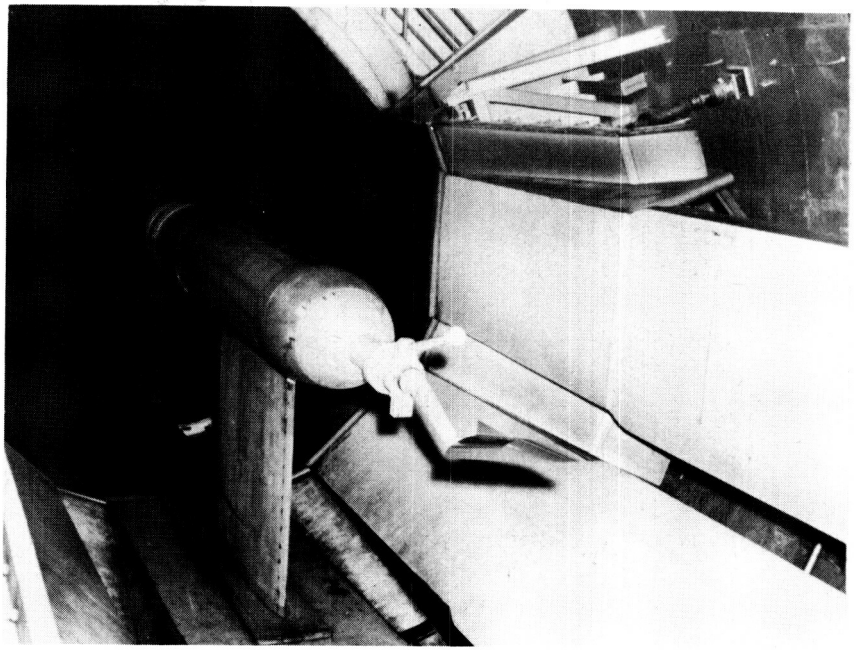

Aspect-ratio-0.62 model L-58-3881

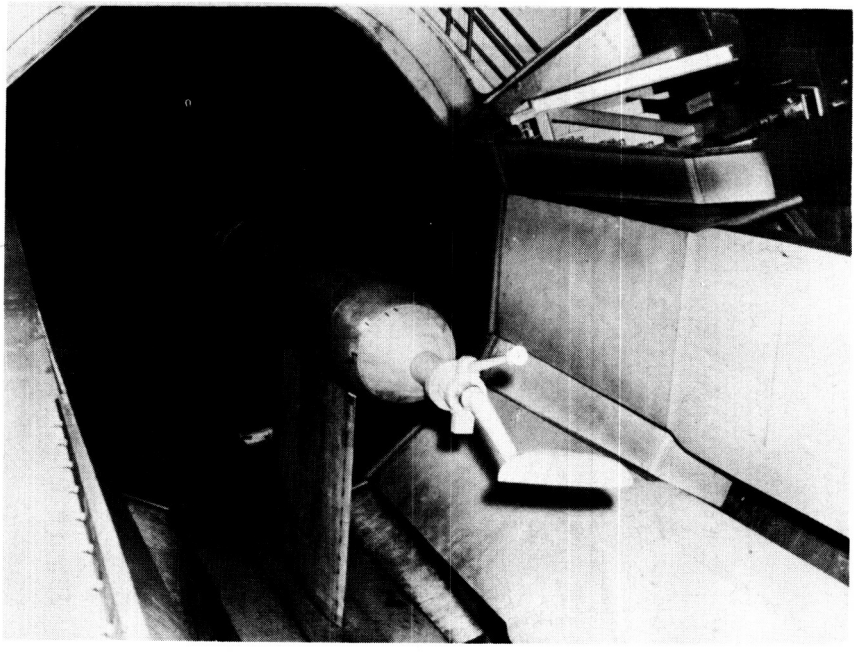

Aspect-ratio-1.25 model L-58-3882

Figure 3.- Photographs of typical setup of models in the Langley 16-foot transonic tunnel.

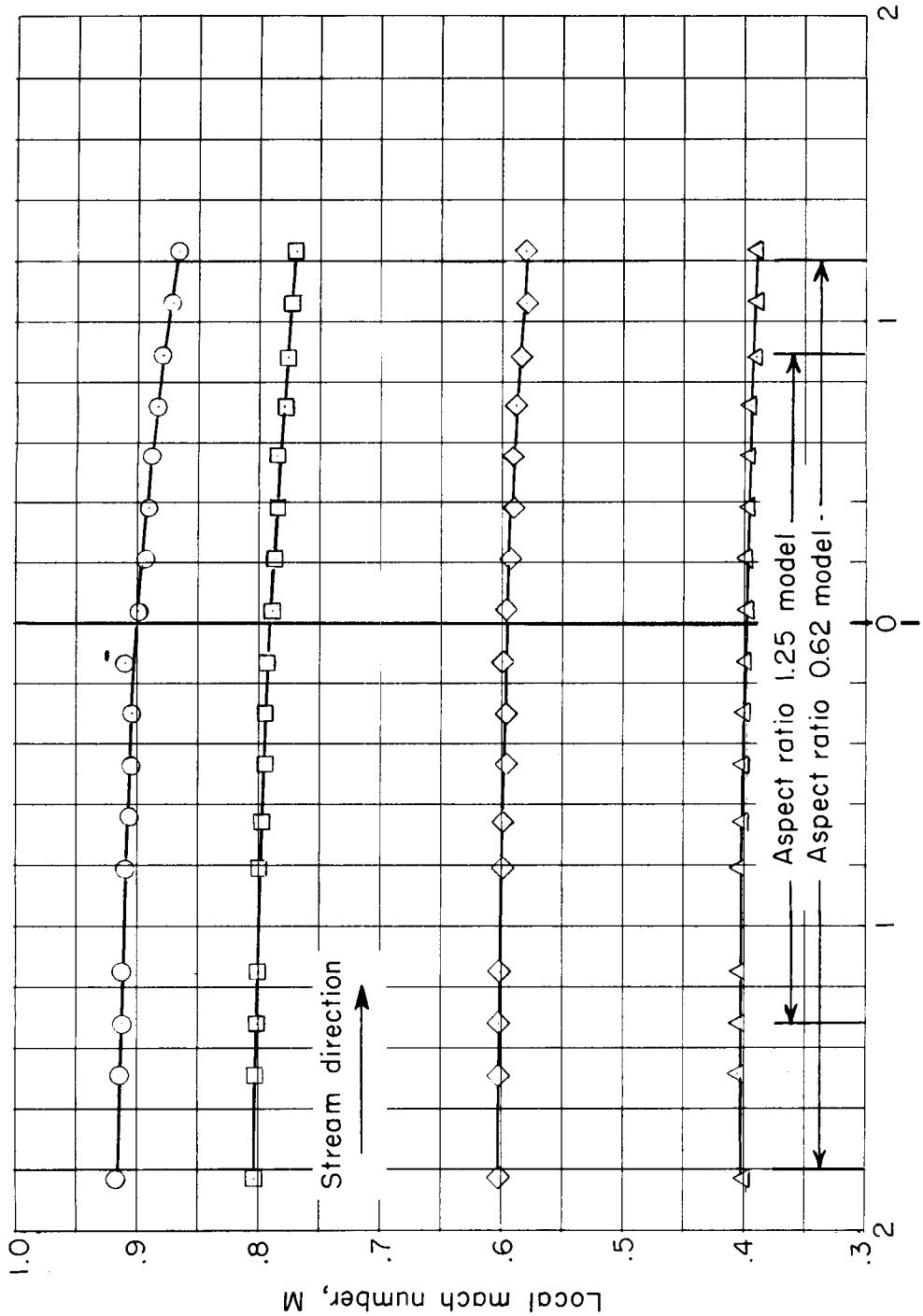

Figure 4.- Variation of free-stream Mach number along model length.

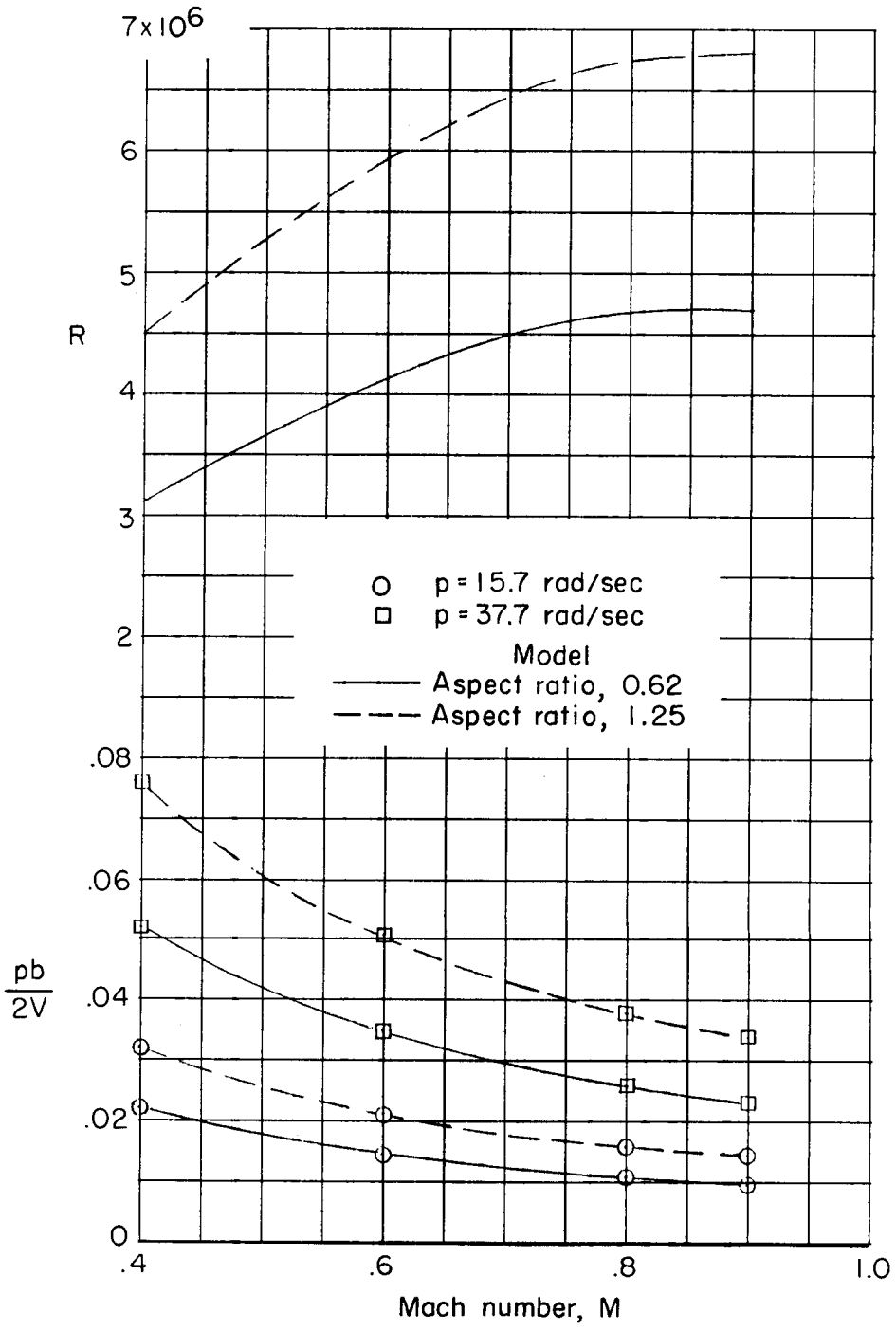

Figure 5.- Variation of maximum and minimum pb/2V for each model and variation of the average test Reynolds number based on the model spans with Mach number.

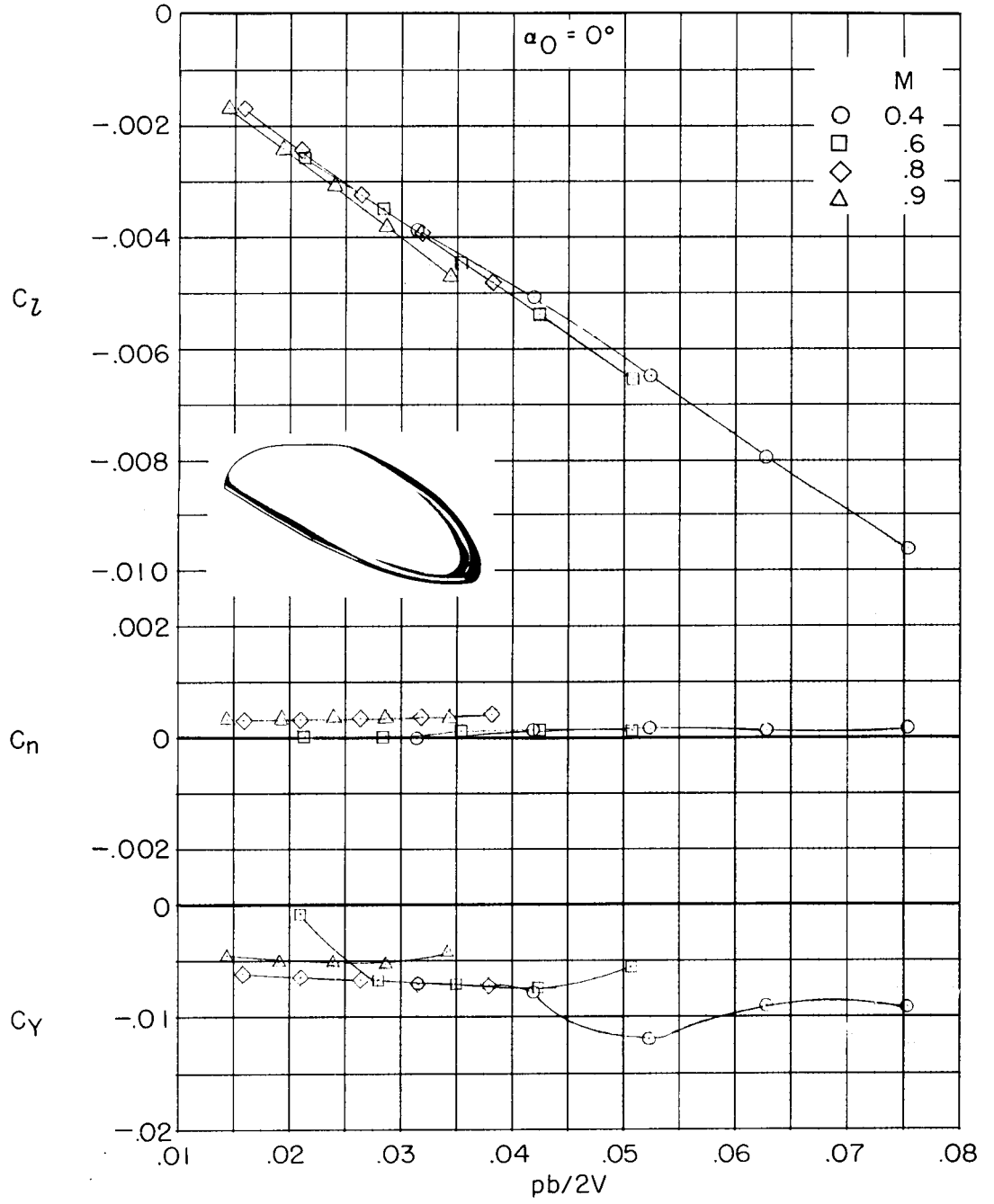

(a) $\alpha_0 = 0°$.

Figure 6.- Variation of rolling-moment, yawing-moment, and side-force coefficients with helix angle for the model with an aspect ratio of 1.25. Body axis.

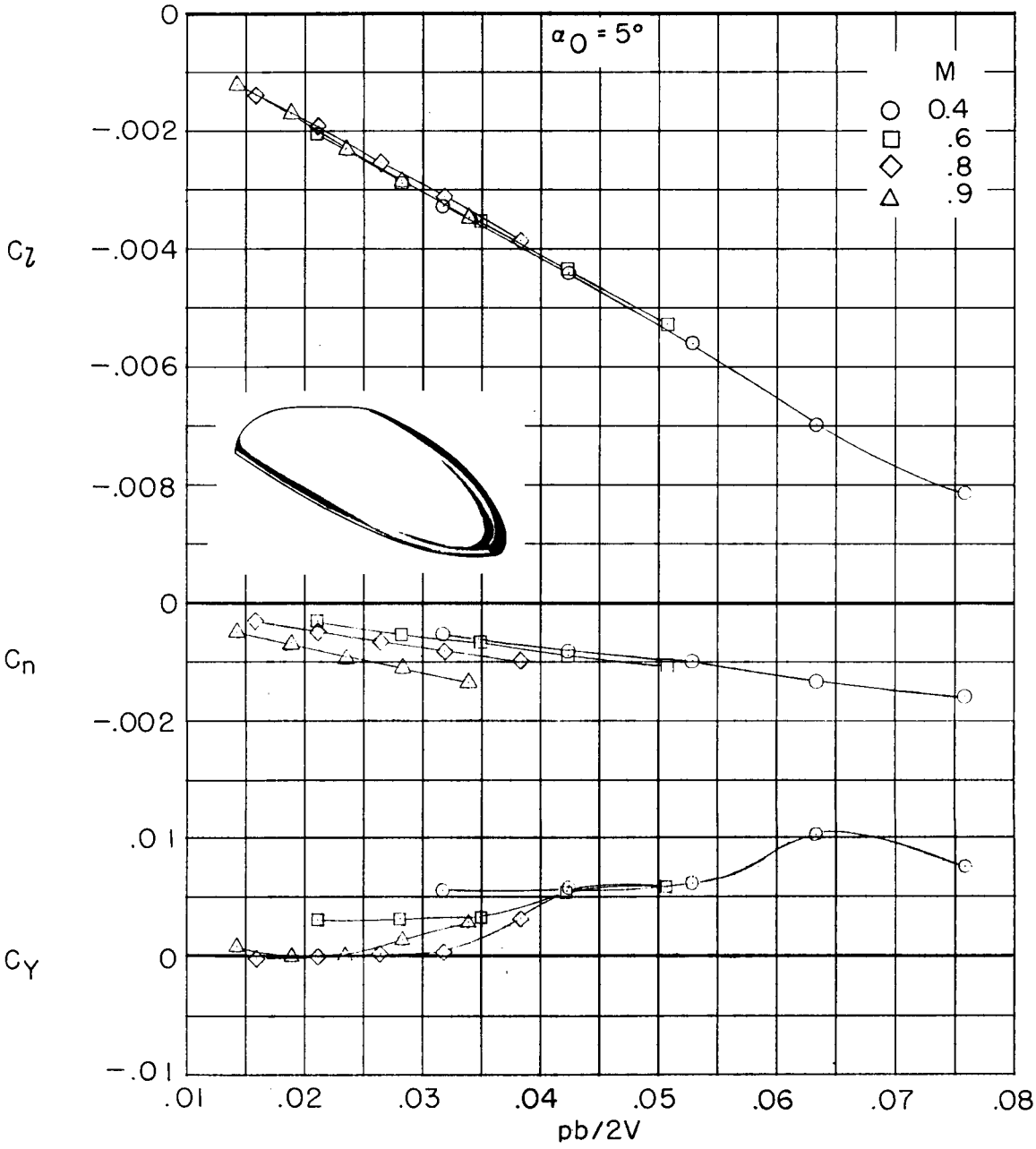

(b) $\alpha_0 = 5°$.

Figure 6.- Continued.

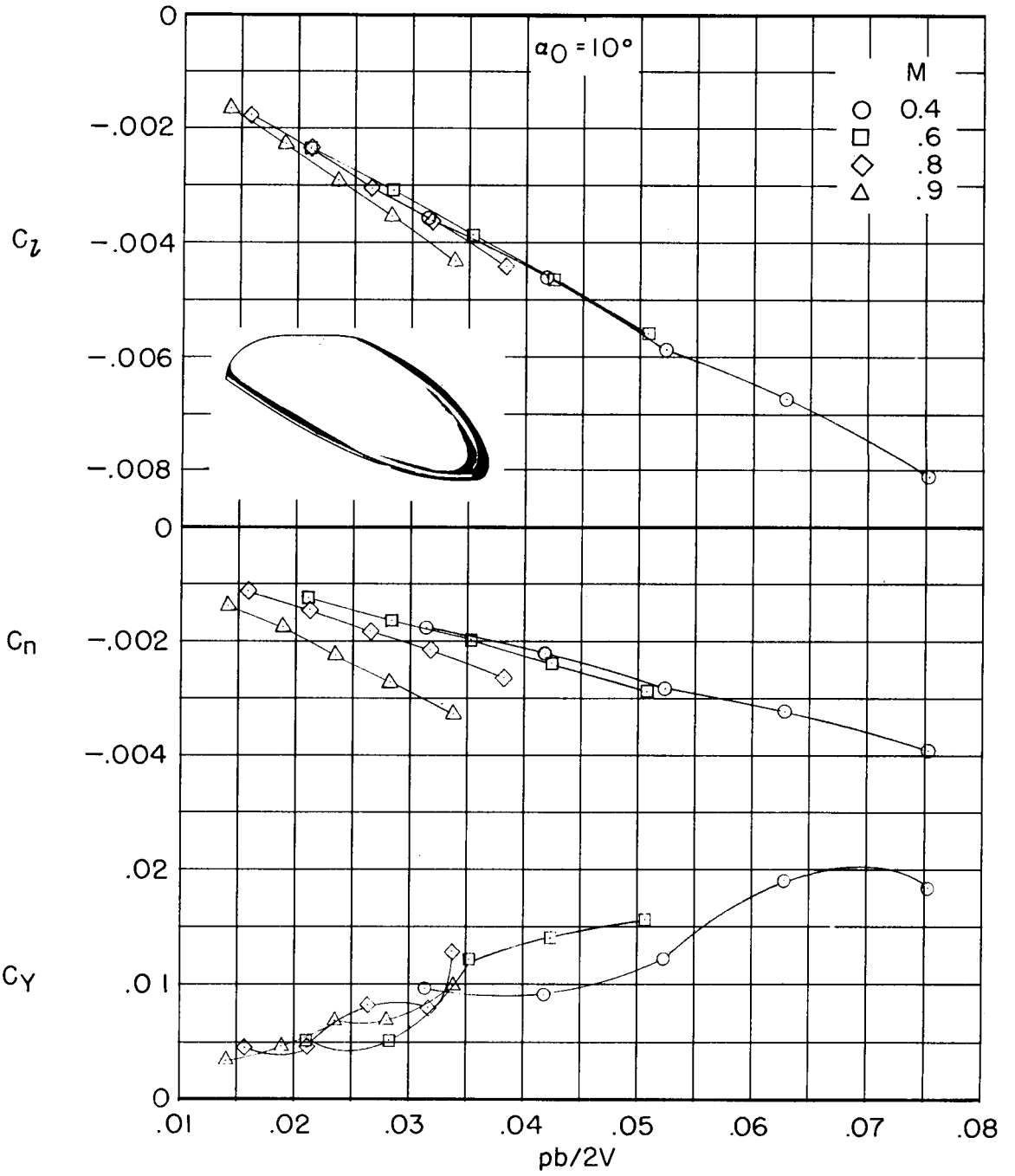

(c) $\alpha_0 = 10°$.

Figure 6.- Continued.

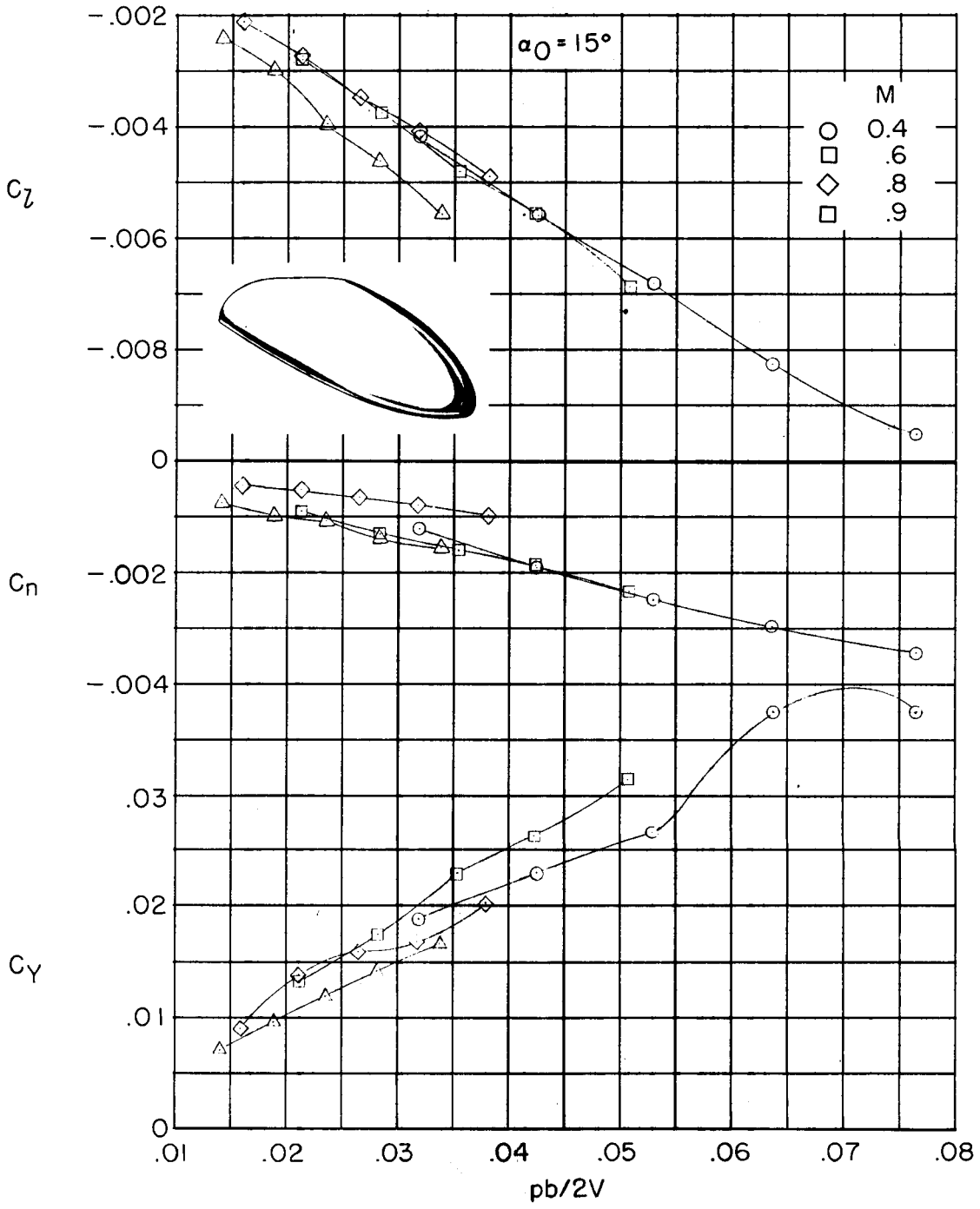

(d) $\alpha_0 = 15°$.

Figure 6.- Concluded.

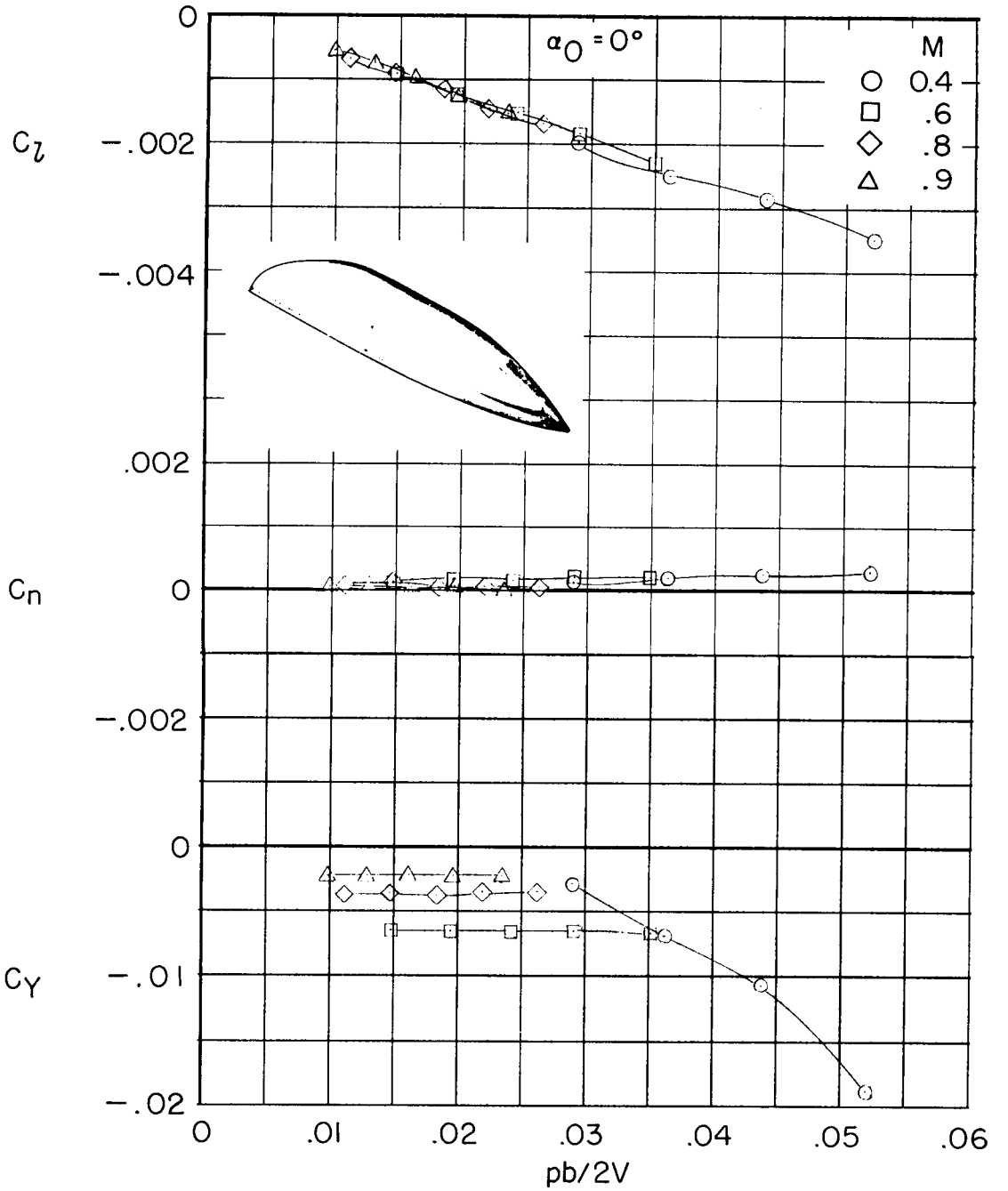

(a) $\alpha_0 = 0°$.

Figure 7.- Variation of rolling-moment, yawing-moment, and side-force coefficients with helix angle for the model with an aspect ratio of 0.62 without a vertical tail. Body axis.

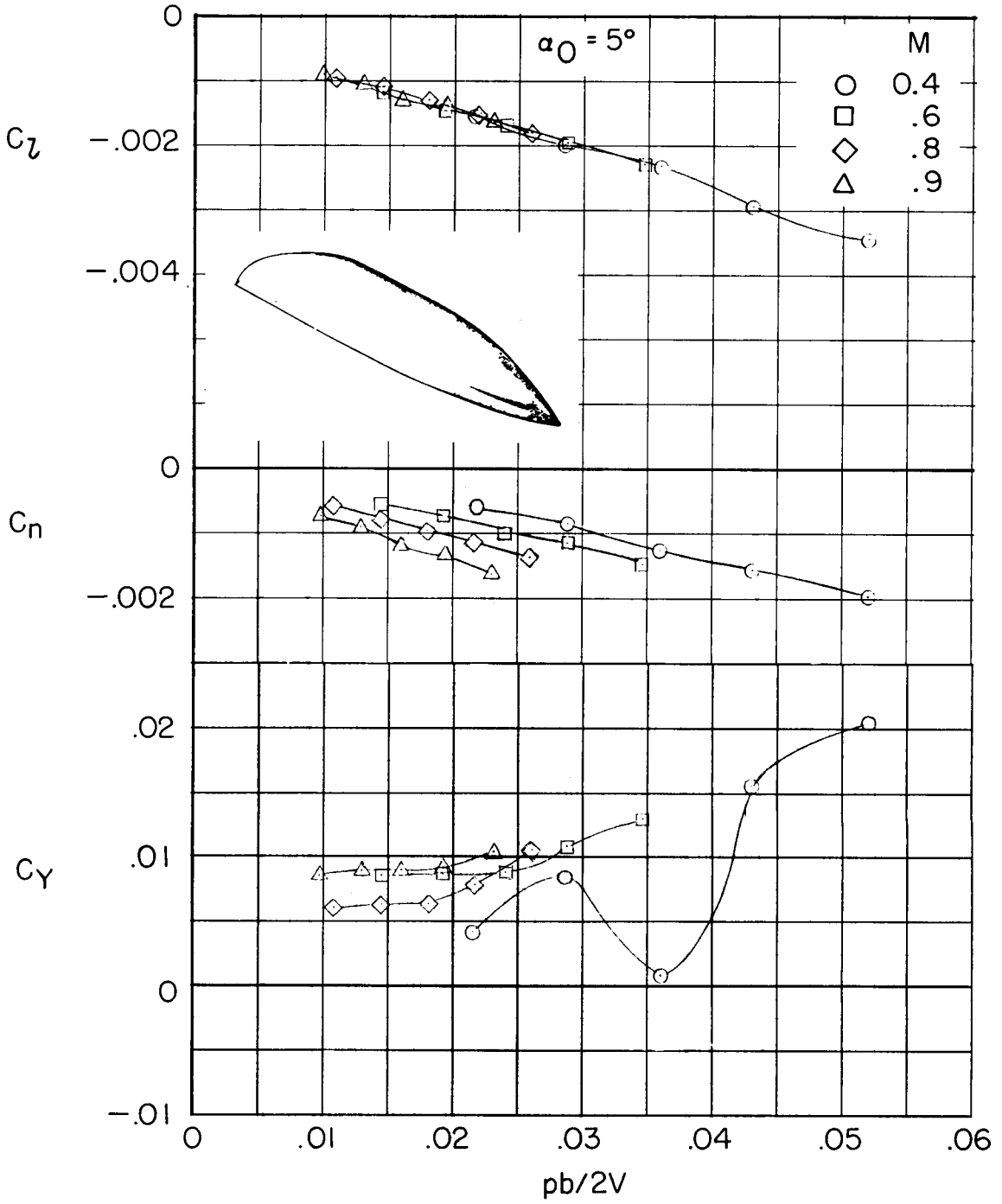

(b) $\alpha_0 = 5°$.

Figure 7.- Continued.

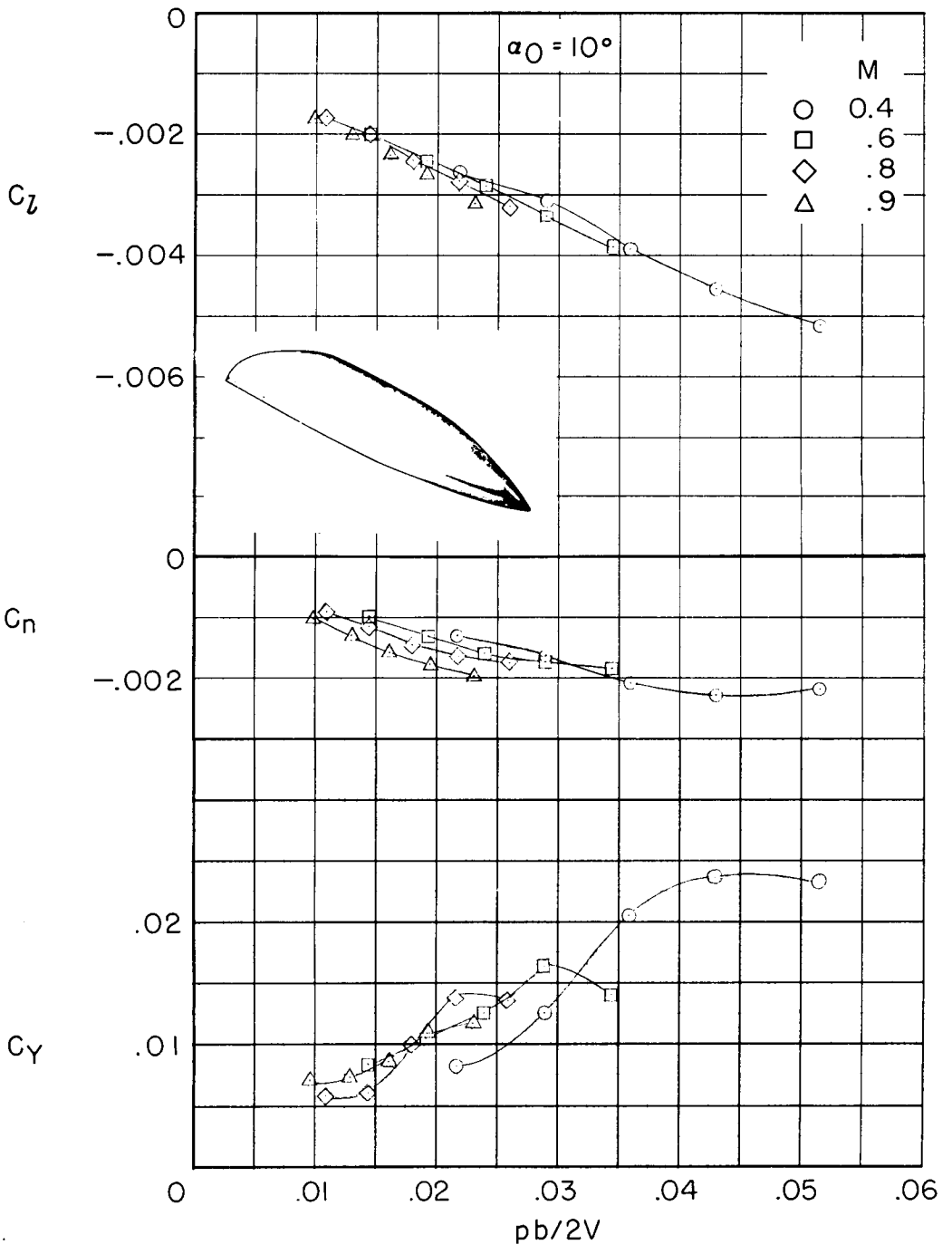

(c) $\alpha_0 = 10°$.

Figure 7.- Continued.

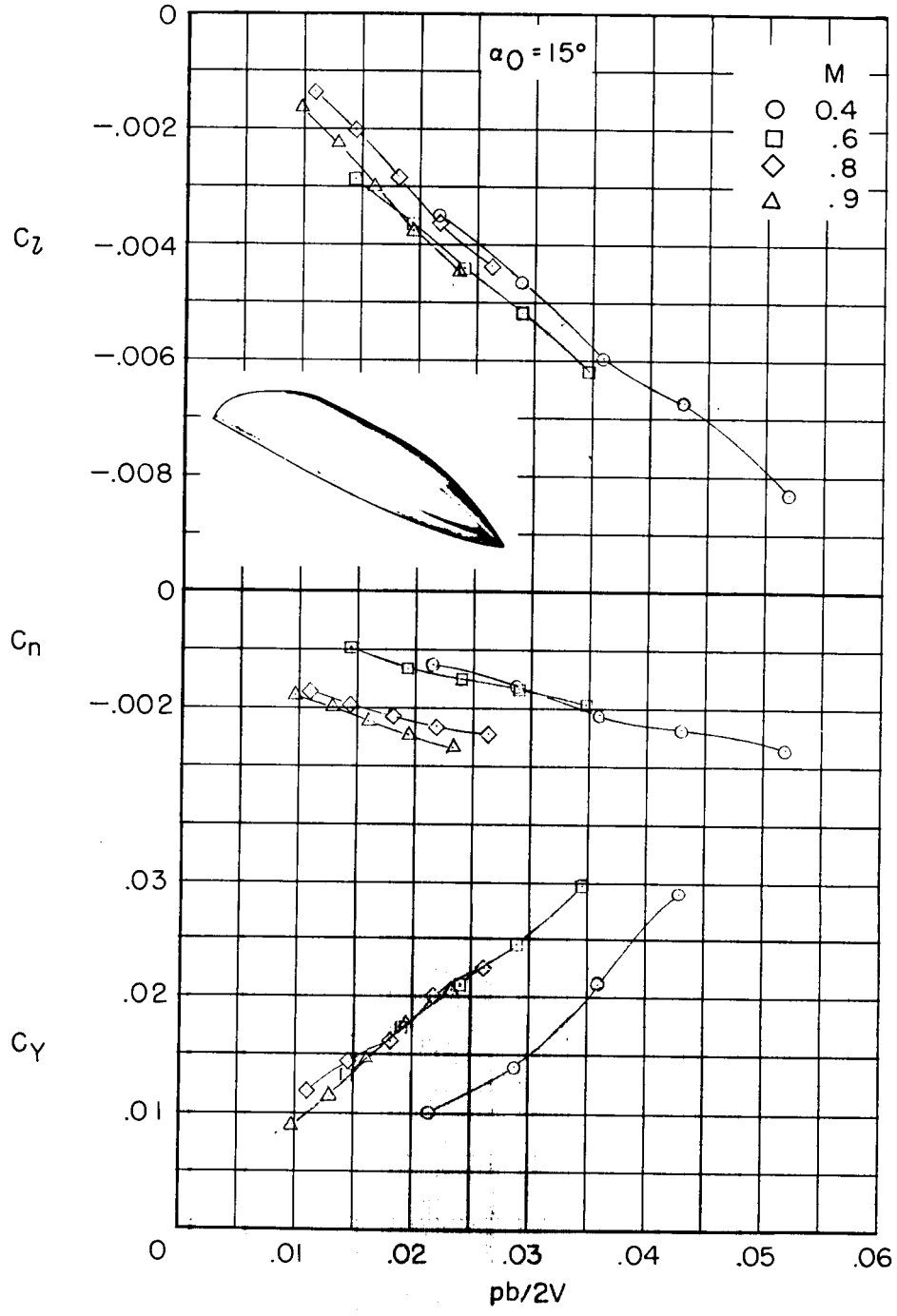

(d) $\alpha_0 = 15°$.

Figure 7.- Concluded.

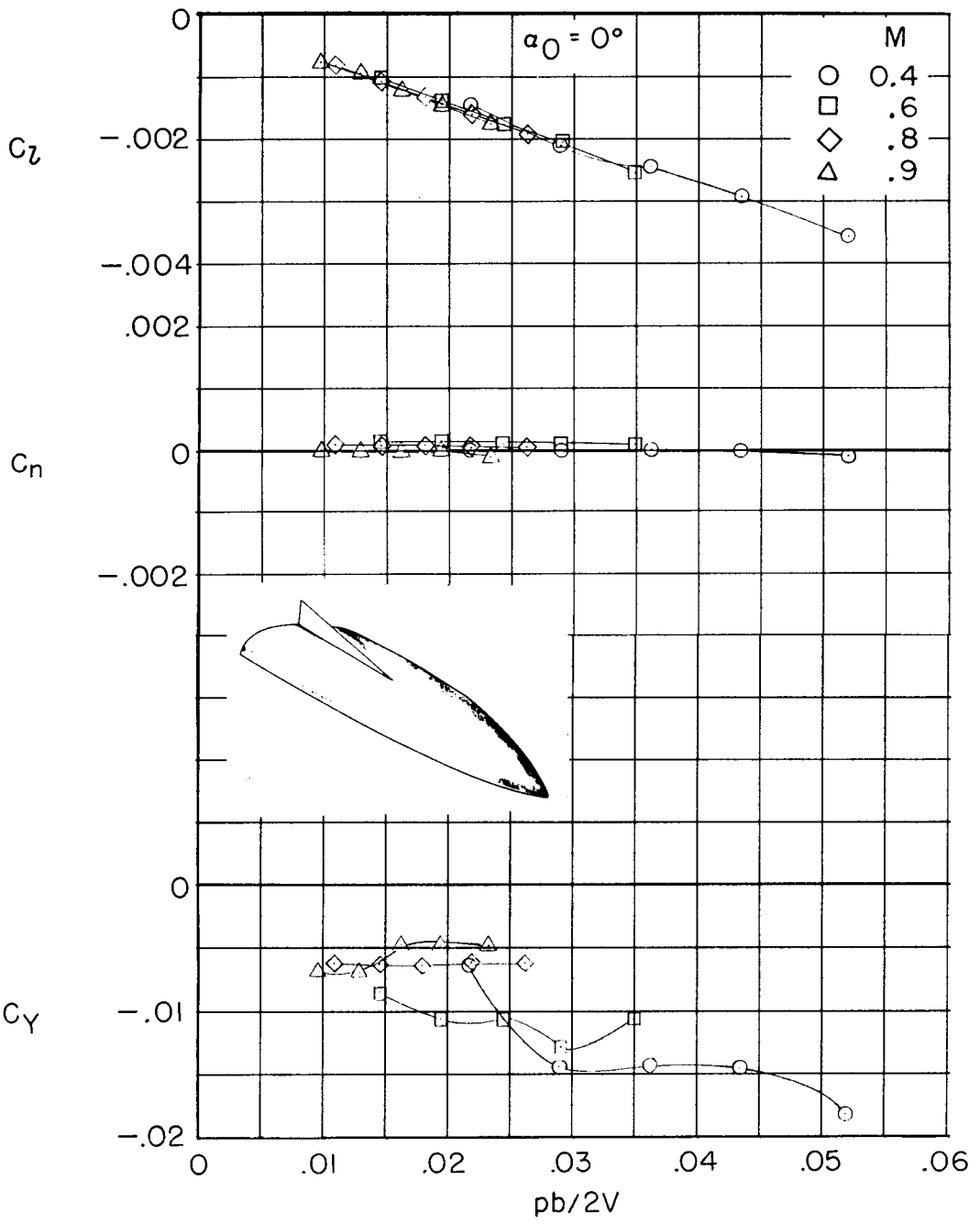

(a) $\alpha_0 = 0°$.

Figure 8.- Variation of rolling-moment, yawing-moment, and side-force coefficients with helix angle for the model with an aspect ratio of 0.62 with a vertical tail. Body axis.

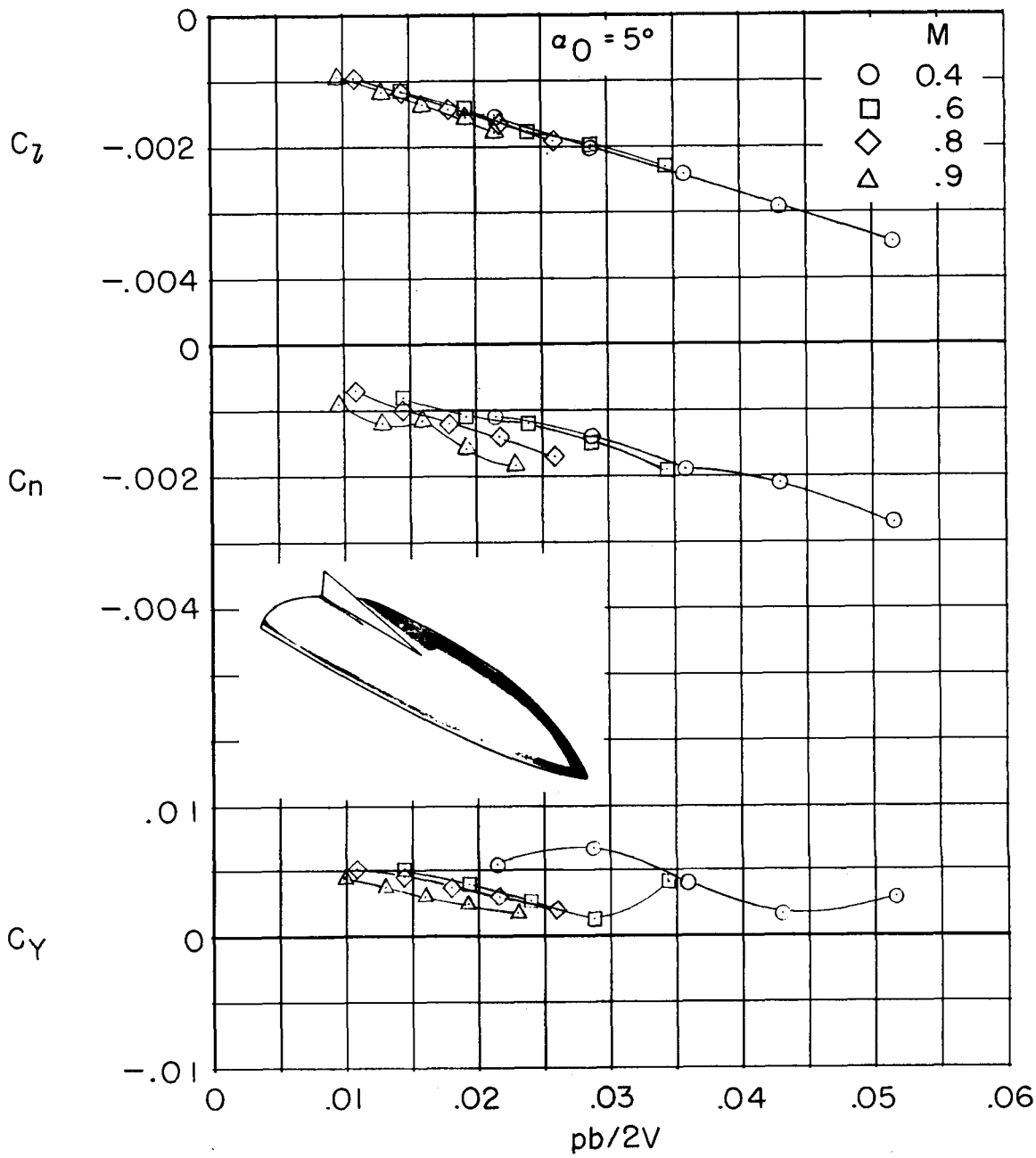

(b) $\alpha_0 = 5°$.

Figure 8.- Continued.

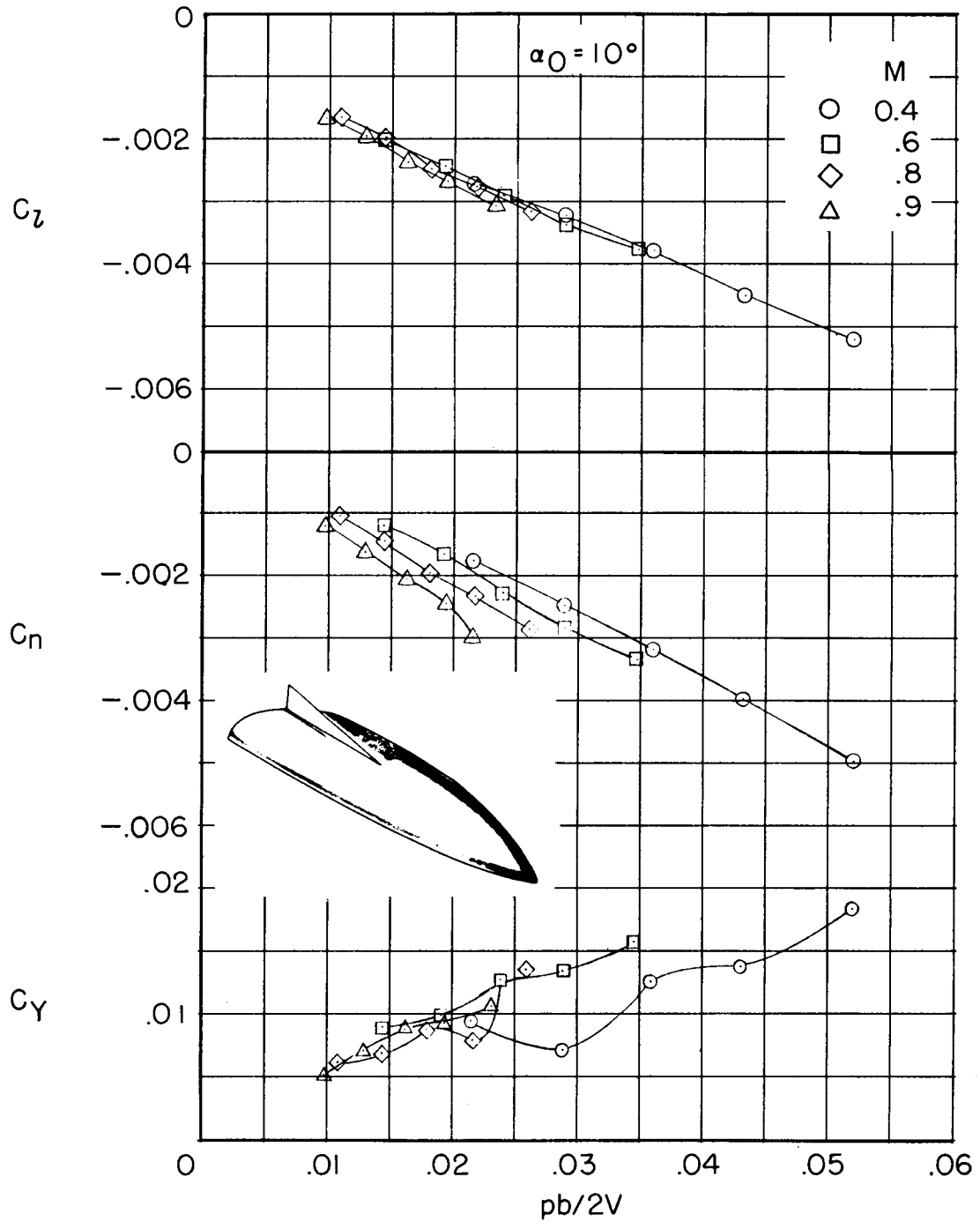

(c) $\alpha_0 = 10°$.

Figure 8.- Continued.

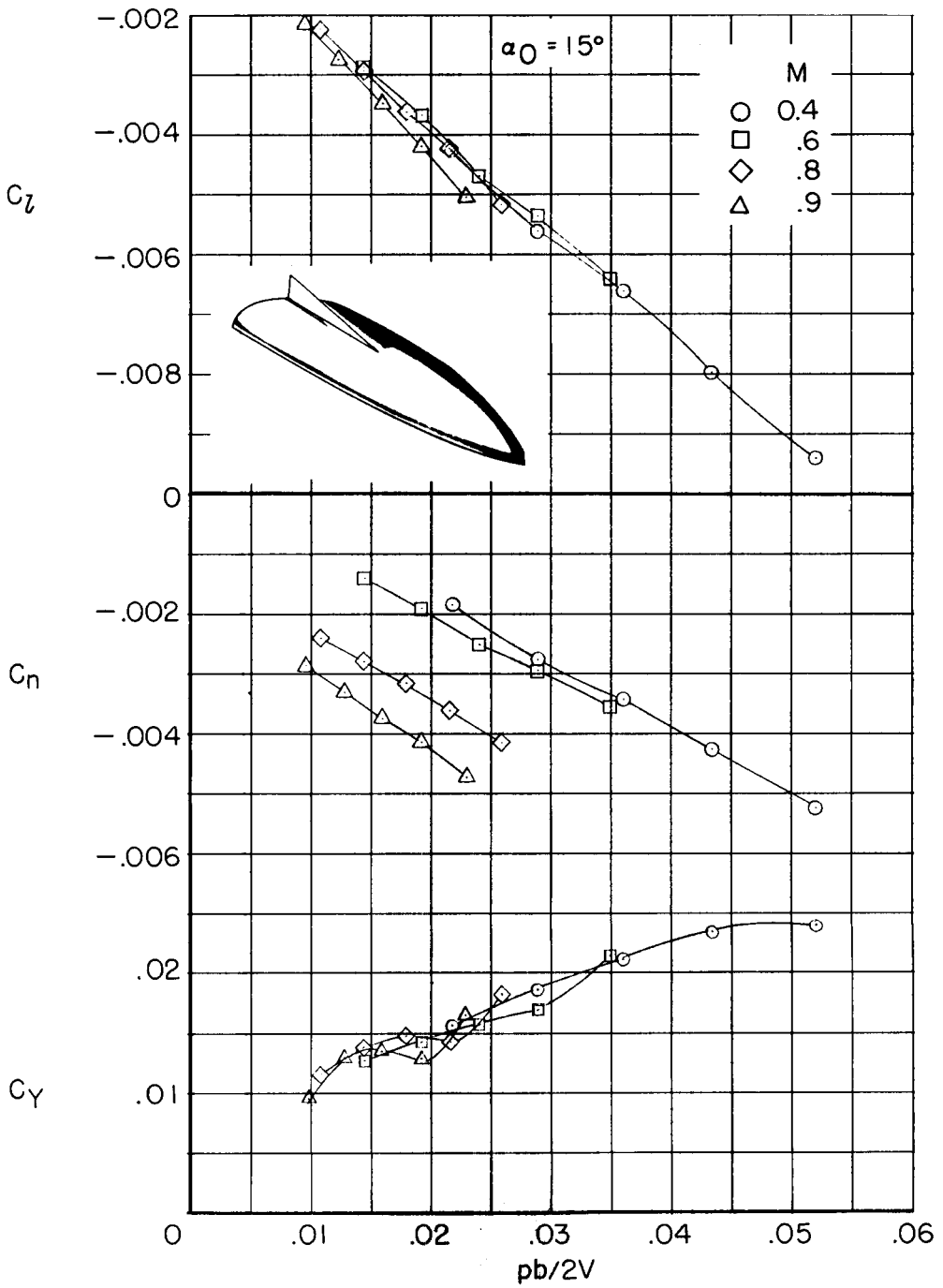

(d) $\alpha_0 = 15°$.

Figure 8.- Concluded.

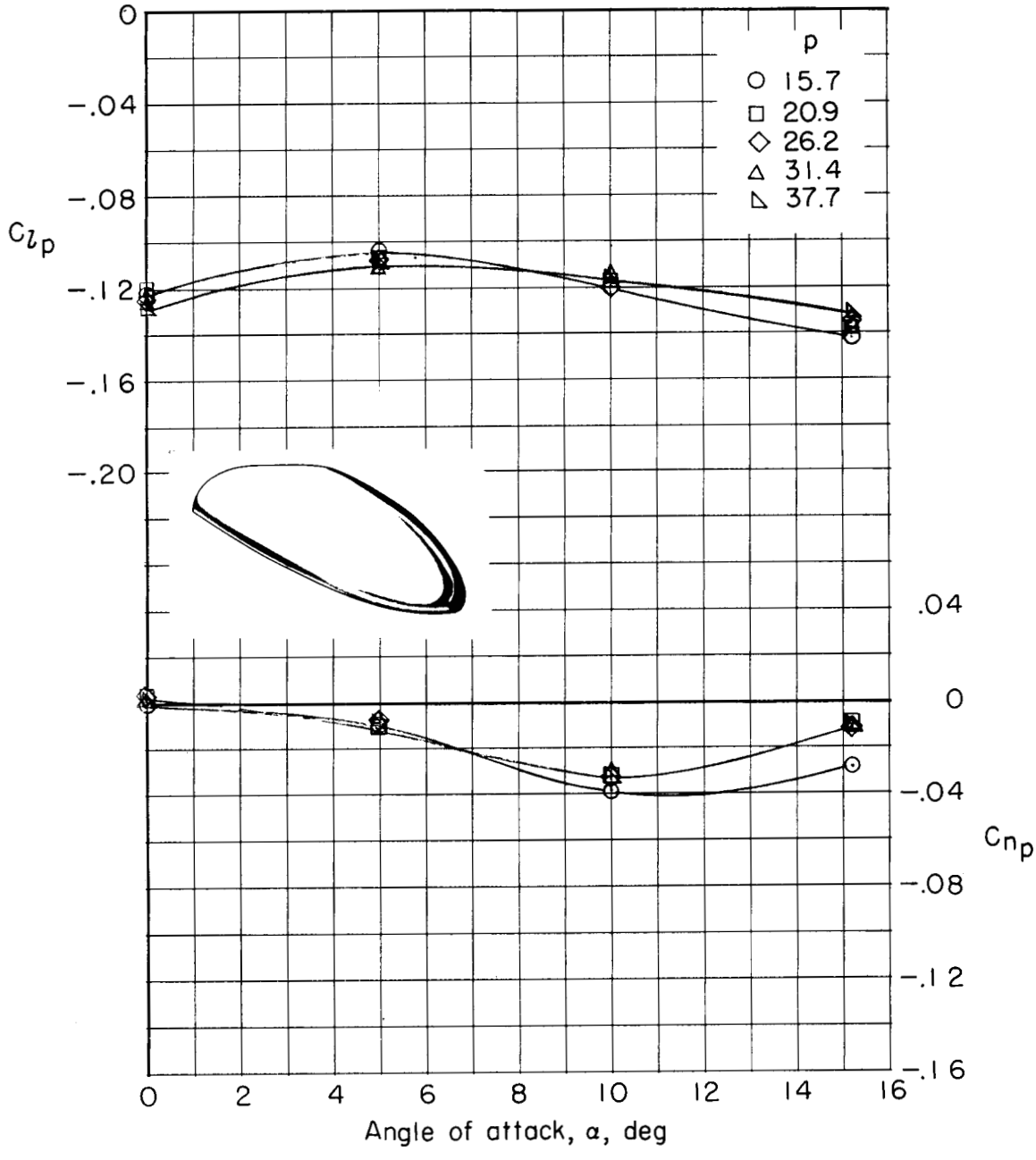

(a) M = 0.40.

Figure 9.- Variation of C_{l_p} and C_{n_p} with angle of attack for a range of roll rates for the model with an aspect ratio of 1.25. Stability axis.

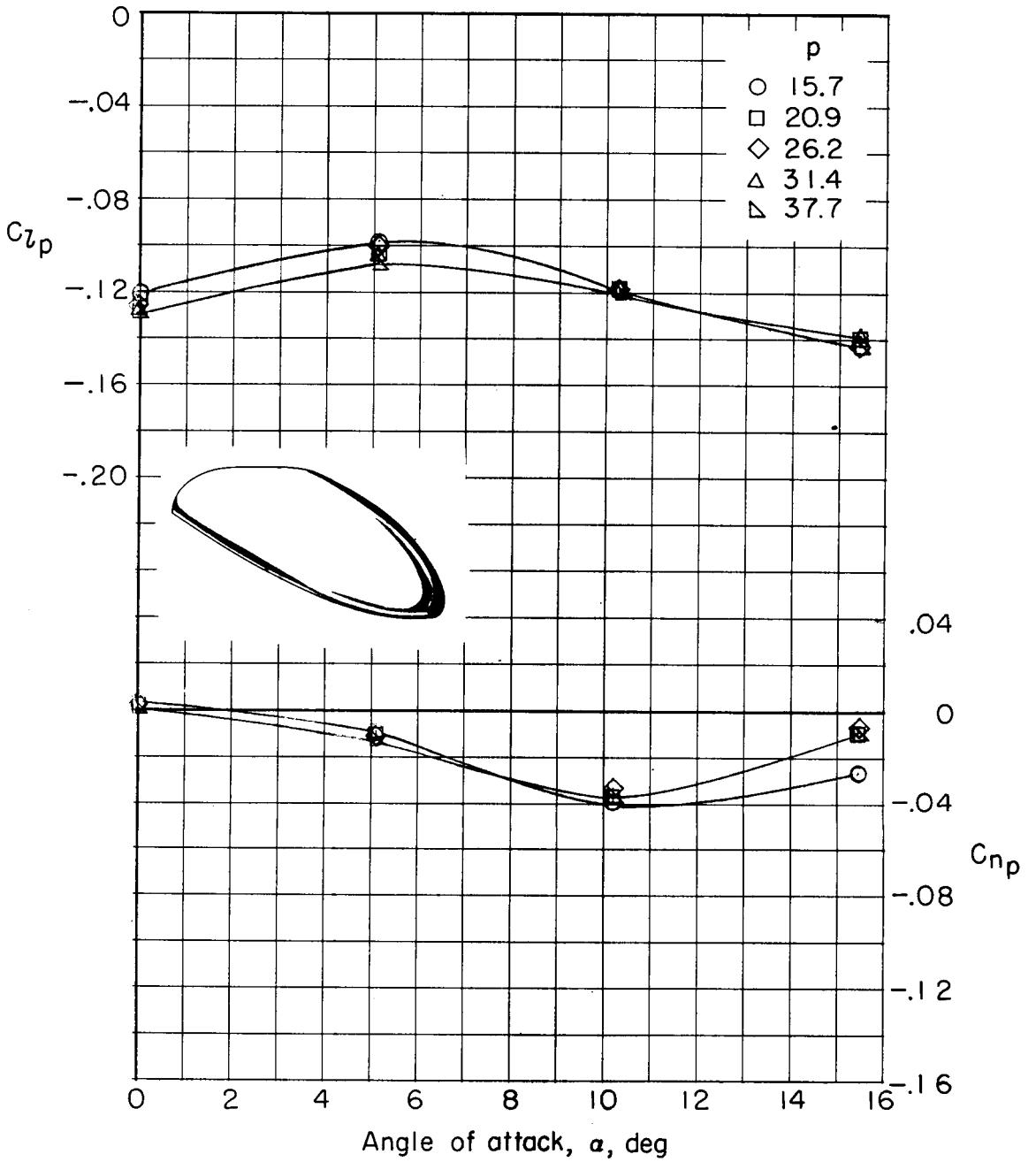

(b) M = 0.60.

Figure 9.- Continued.

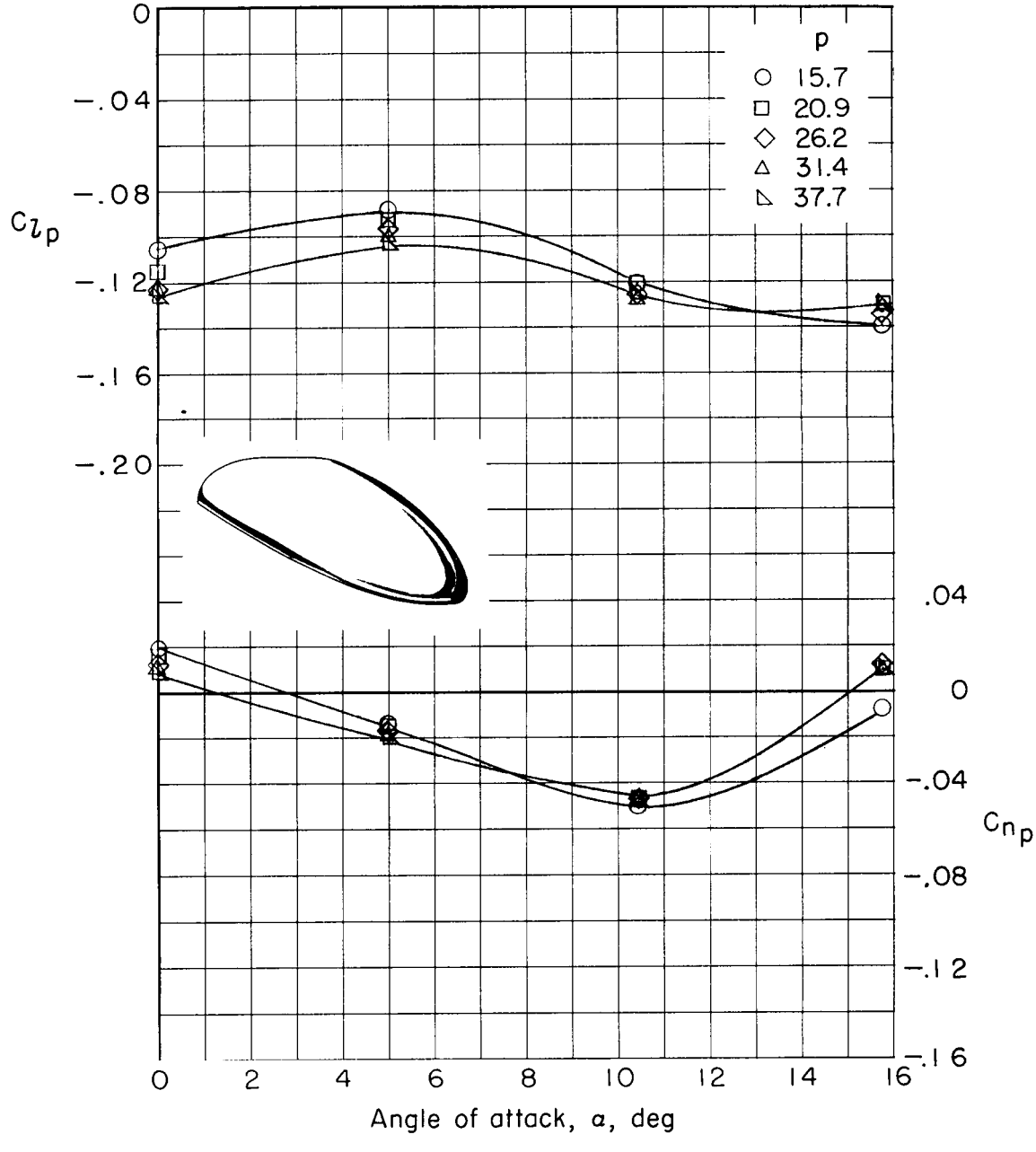

(c) M = 0.80.

Figure 9.- Continued.

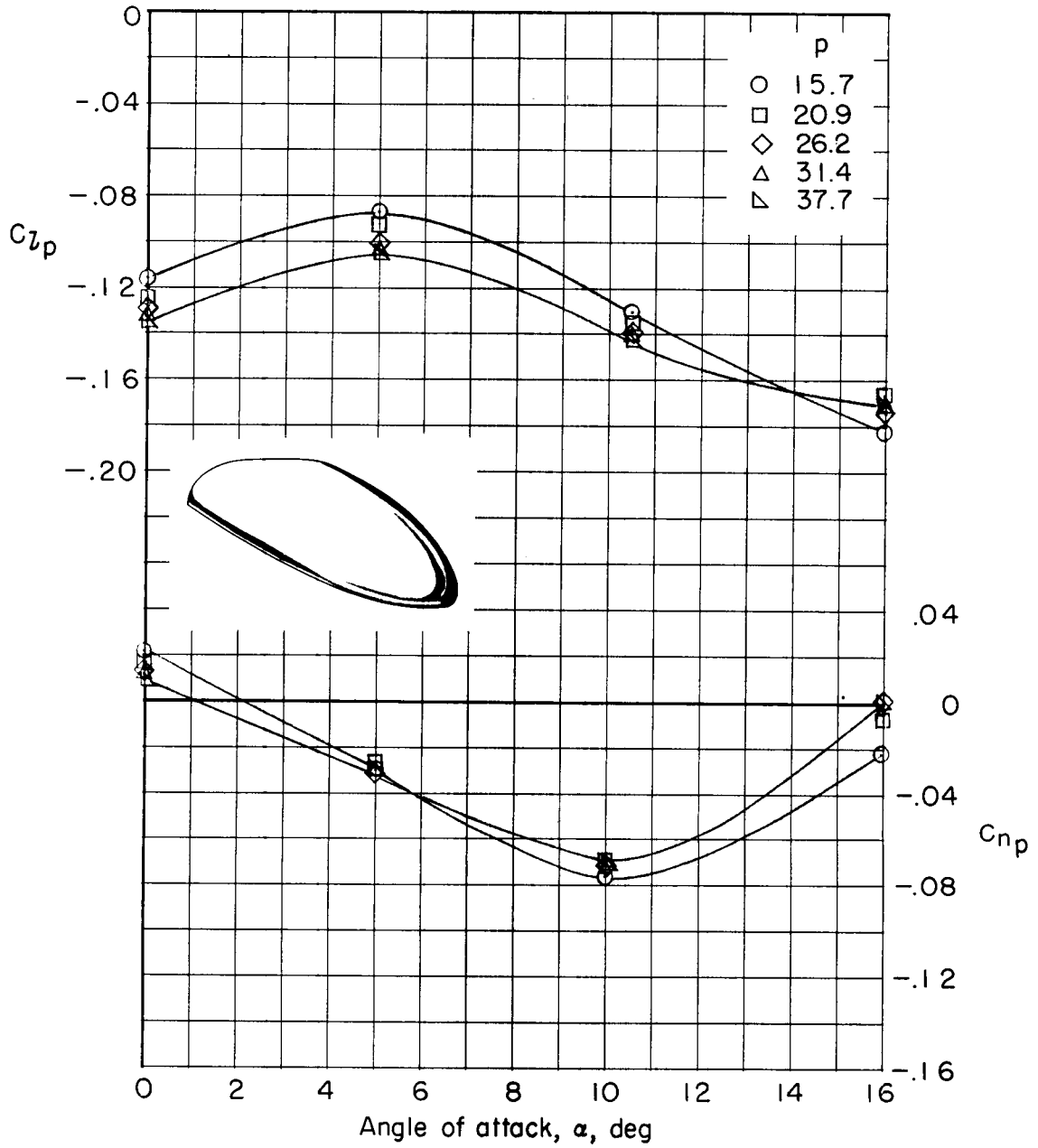

(d) M = 0.90.

Figure 9.- Concluded.

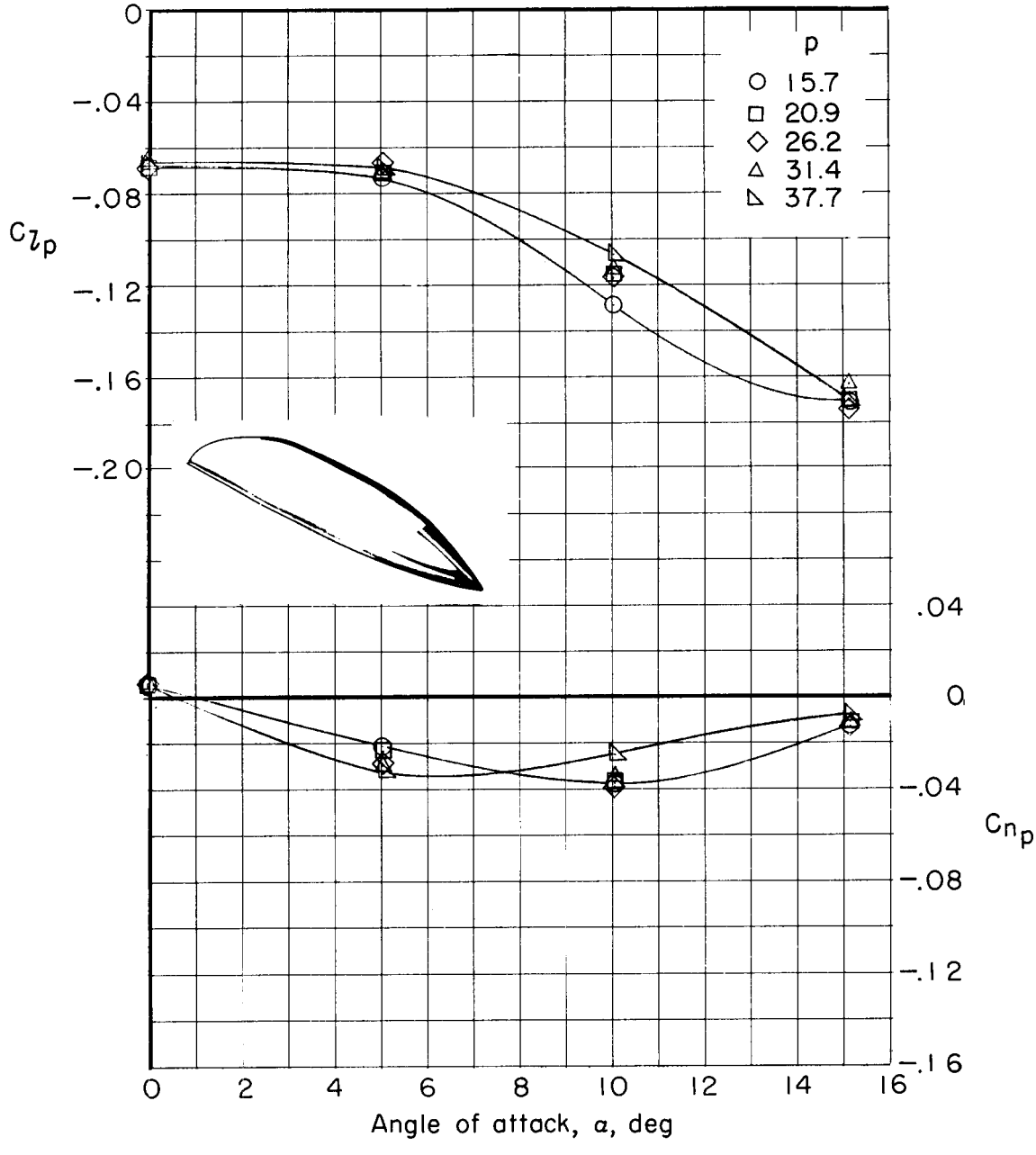

(a) M = 0.40.

Figure 10.- Variation of C_{l_p} and C_{n_p} with angle of attack for a rang of roll rates for the model with an aspect ratio of 0.62 without a vertical tail. Stability axis.

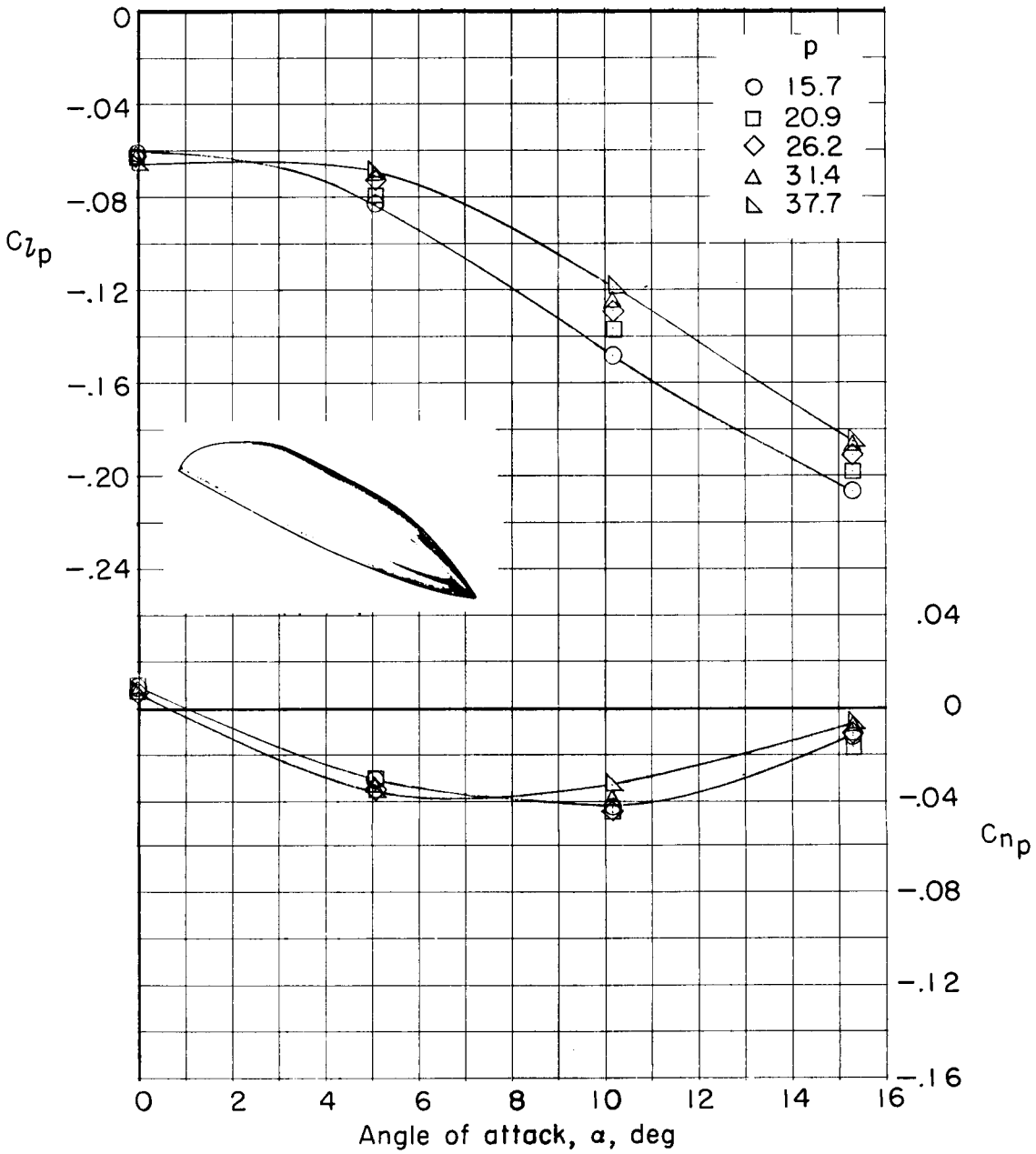

(b) M = 0.60.

Figure 10.- Continued.

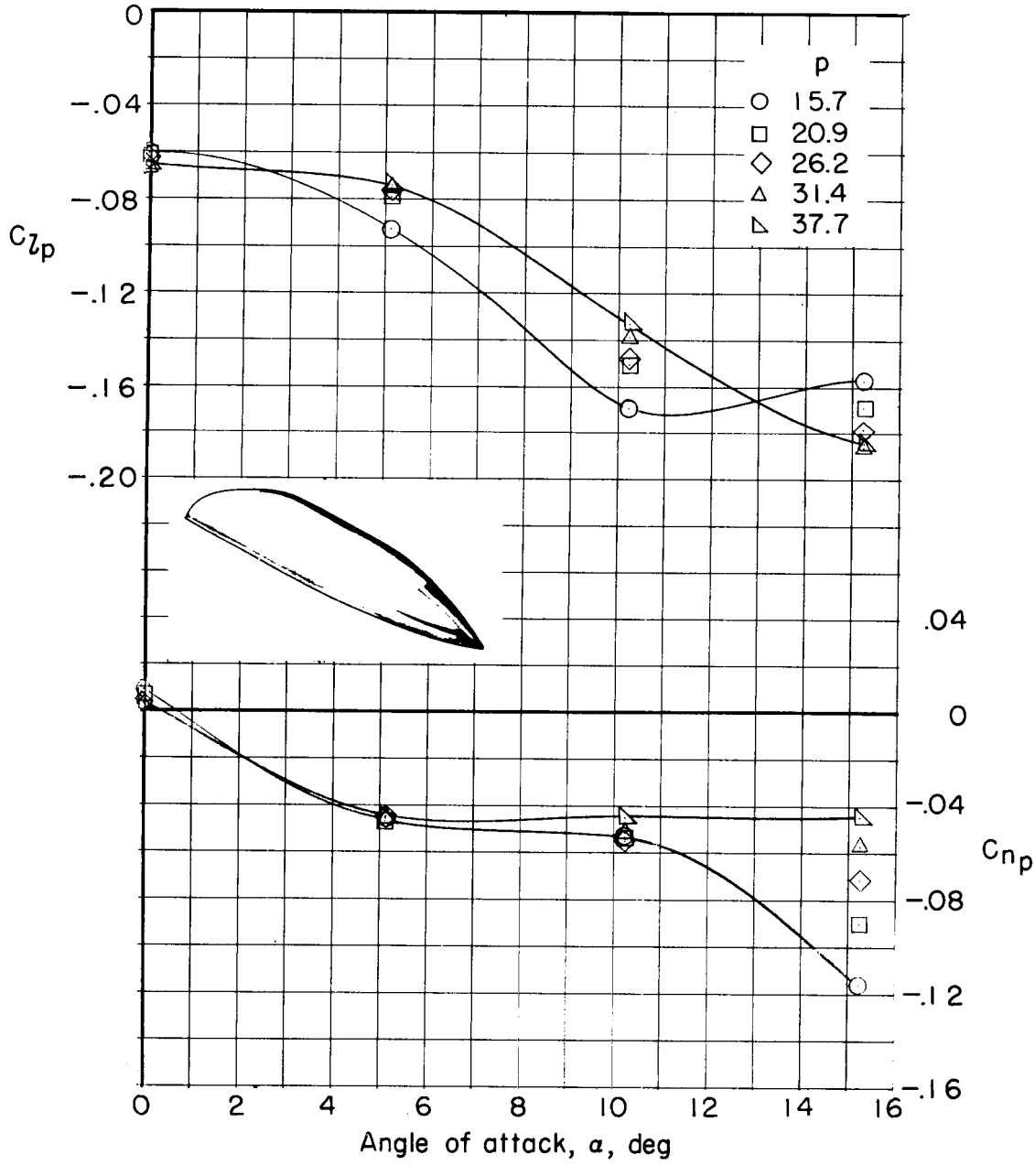

(c) M = 0.80.

Figure 10.- Continued.

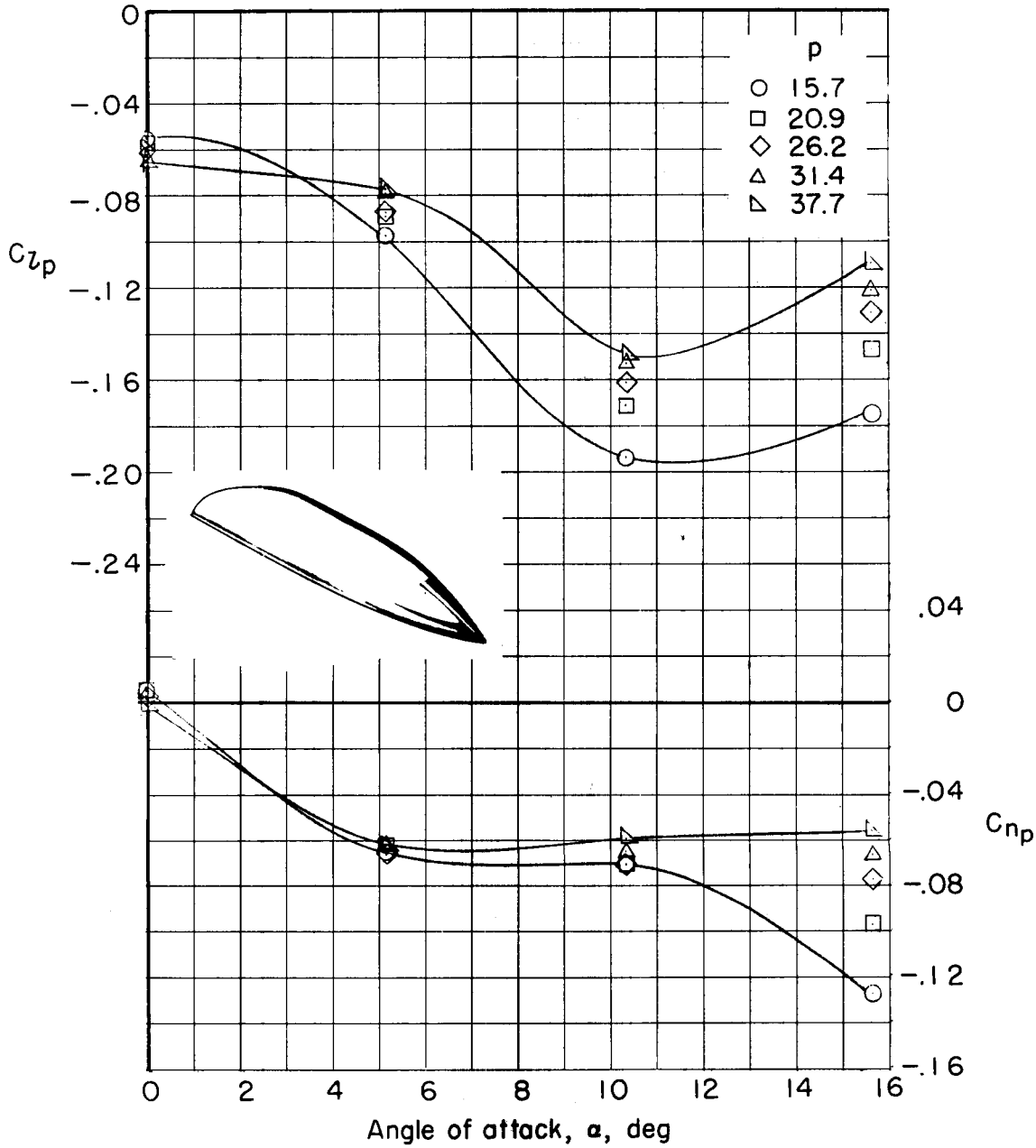

(d) M = 0.90.

Figure 10.- Concluded.

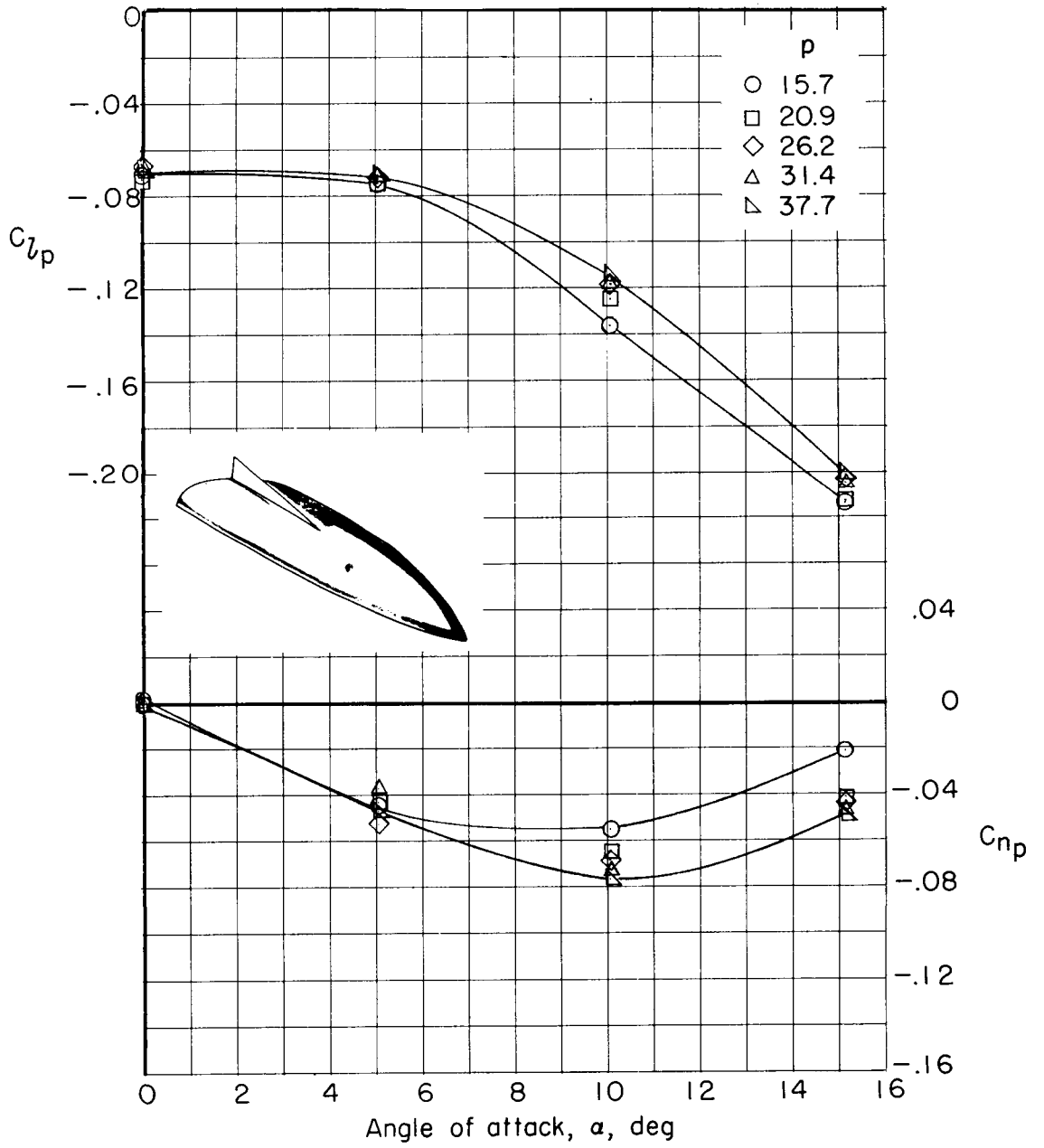

(a) M = 0.40.

Figure 11.- Variation of the stability derivatives C_{l_p} and C_{n_p} with angle of attack for a range of roll rates for the model with an aspect ratio of 0.62 with a vertical tail. Stability axis.

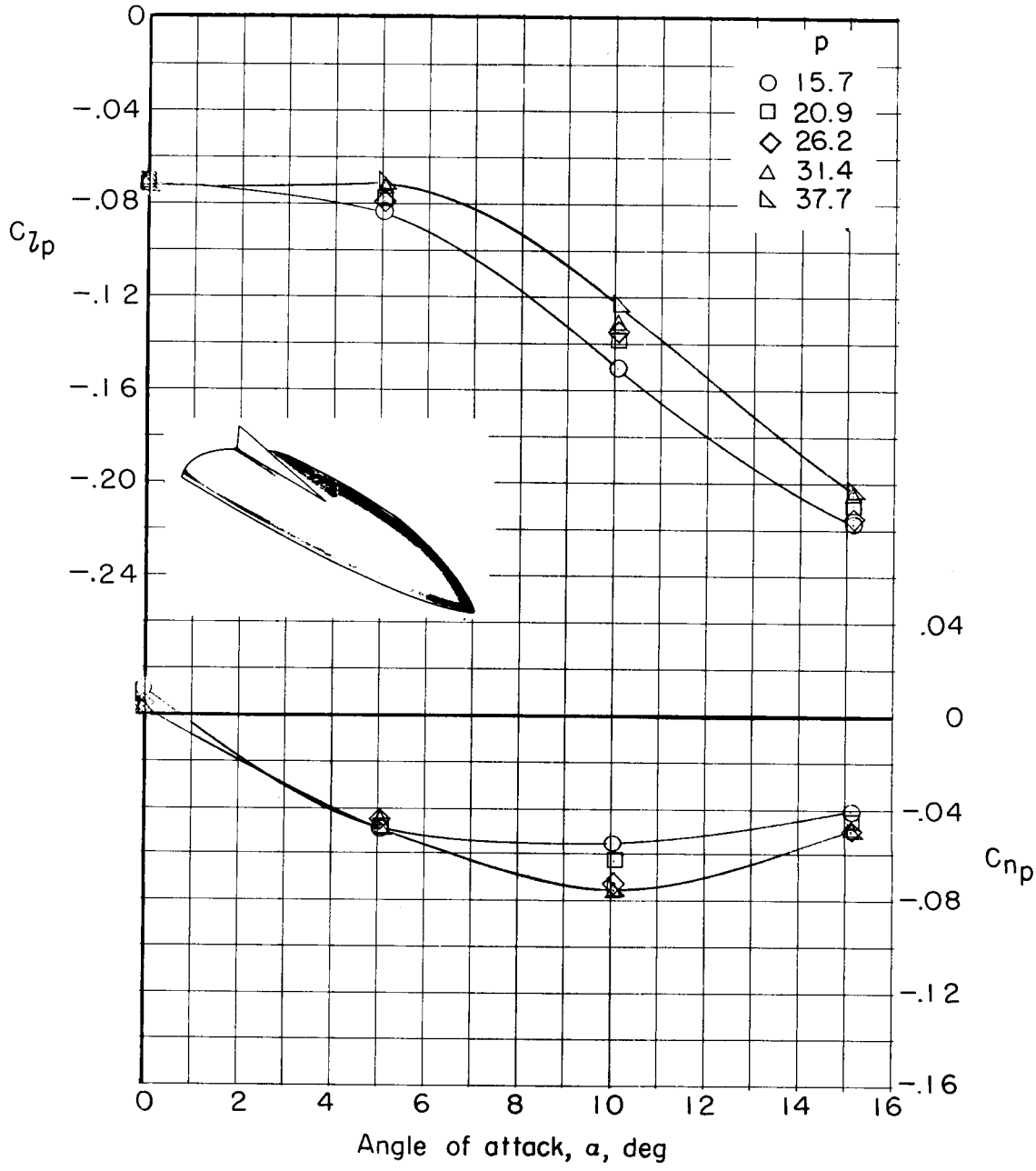

(b) M = 0.60.

Figure 11.- Continued.

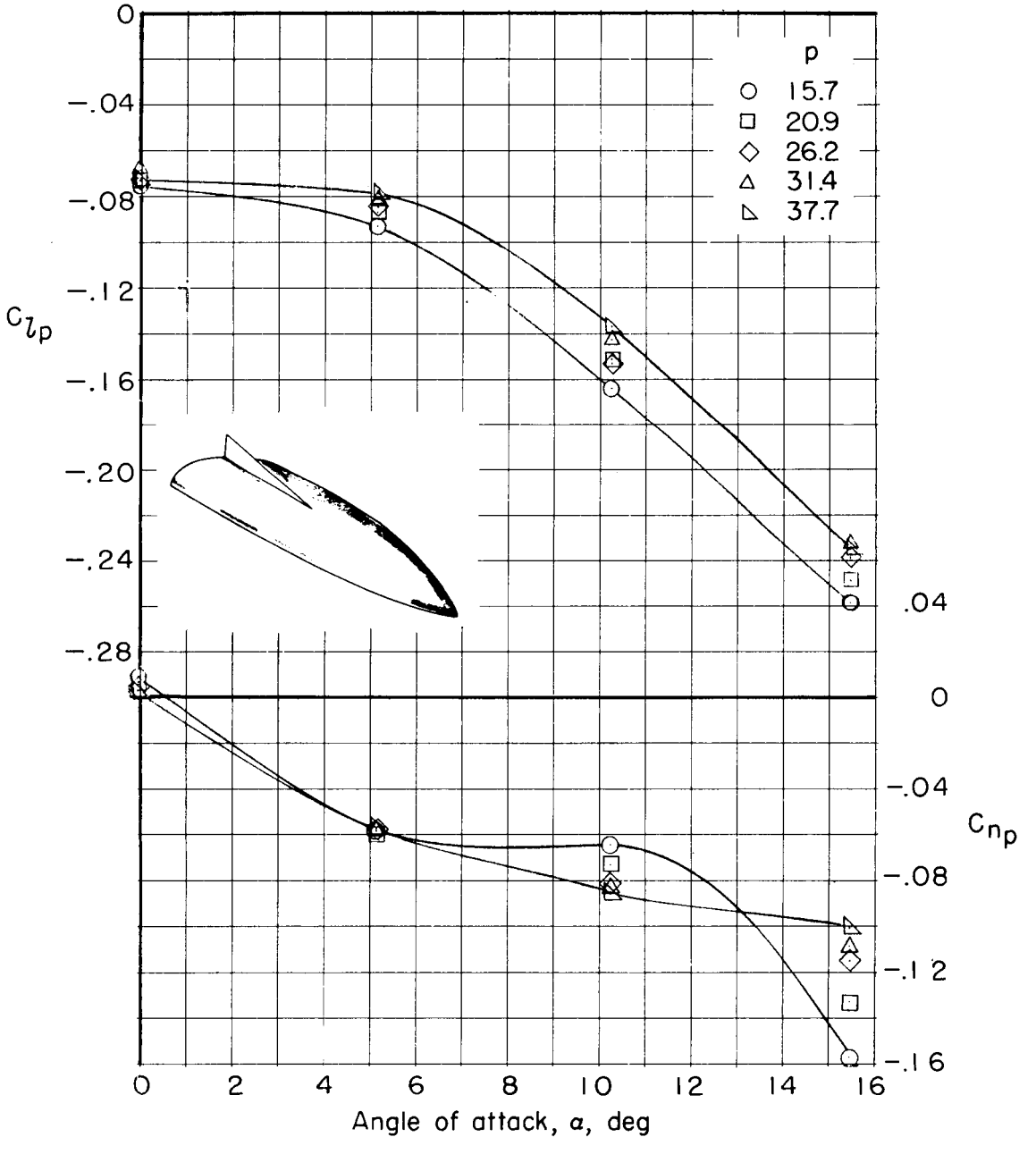

(c) M = 0.80.

Figure 11.- Continued.

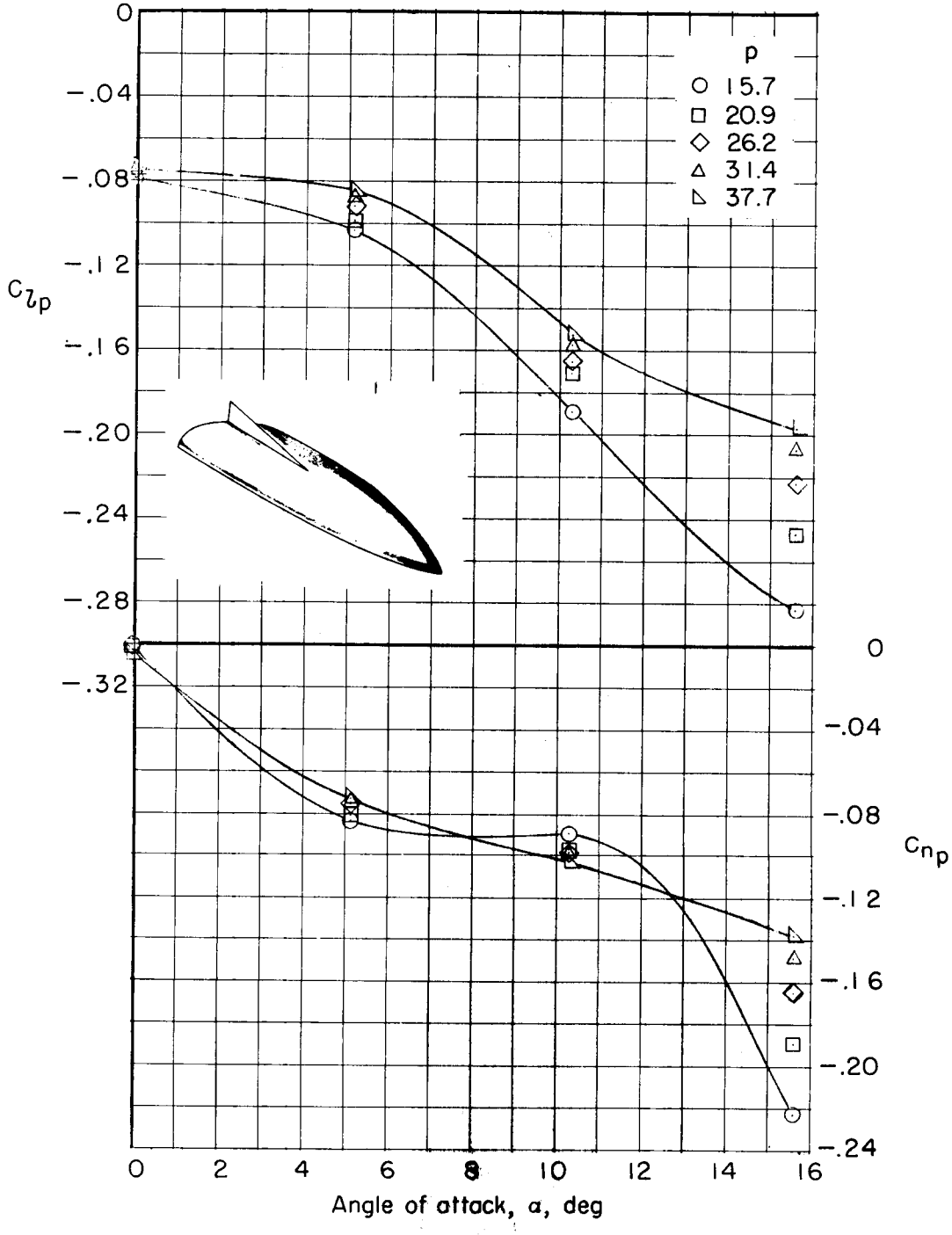

(d) M = 0.90.

Figure 11.- Concluded.

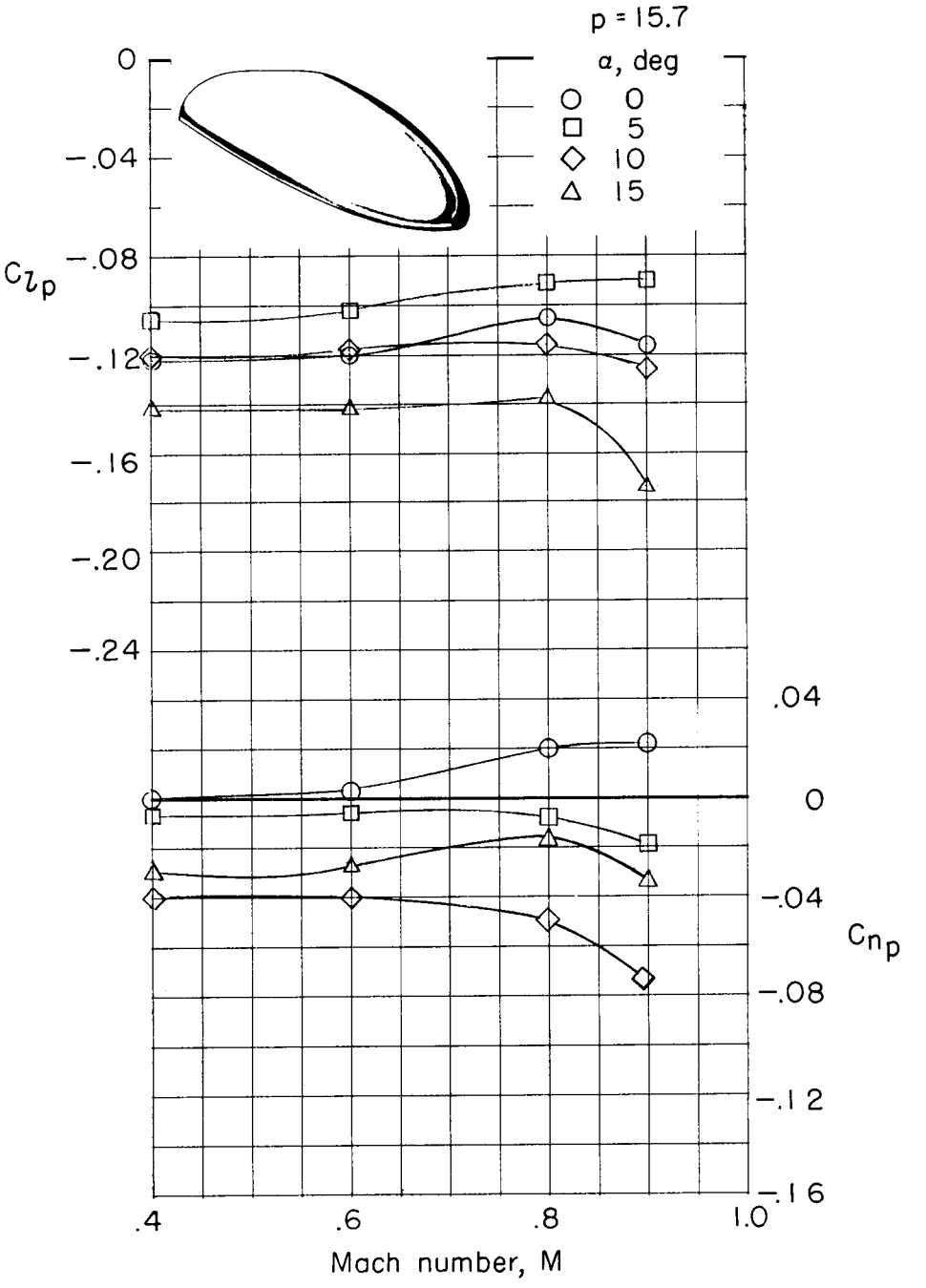

(a) Aspect-ratio-1.25 model.

Figure 12.- Variation of C_{l_p} and C_{n_p} with Mach number. Stability axis.

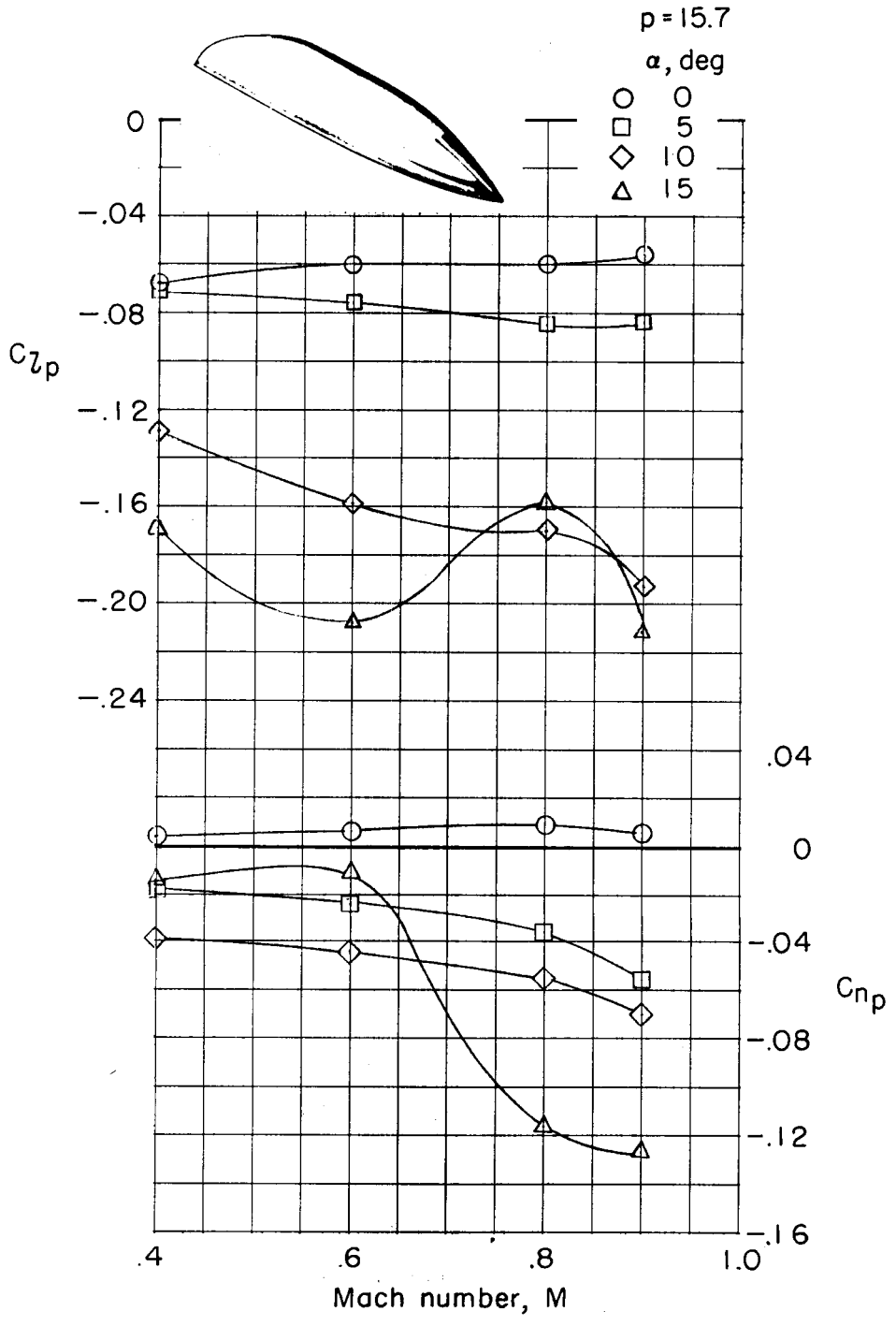

(b) Aspect-ratio-0.62 model without tail.

Figure 12.- Continued.

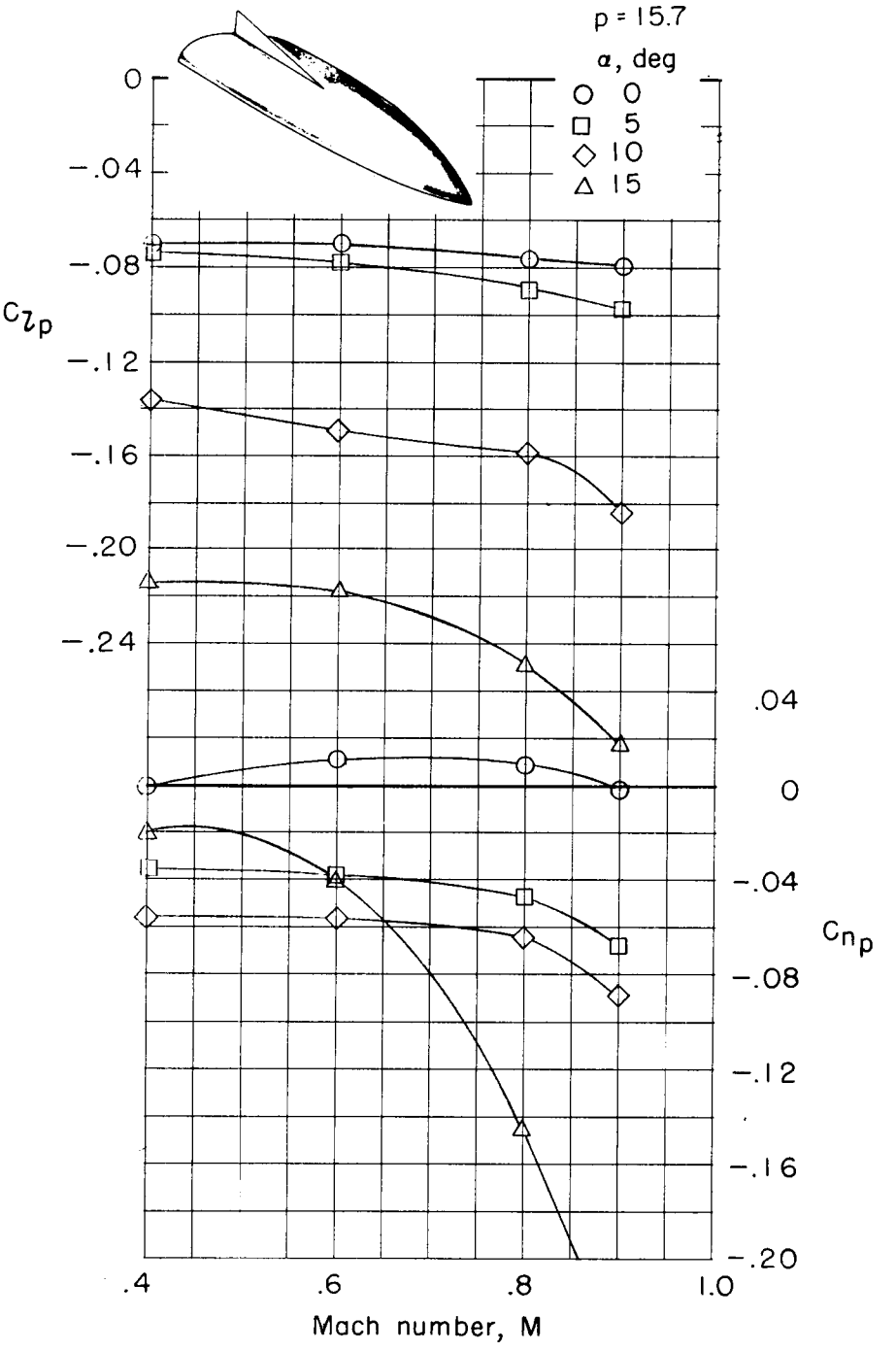

(c) Aspect-ratio-0.62 model with tail.

Figure 12.- Concluded.

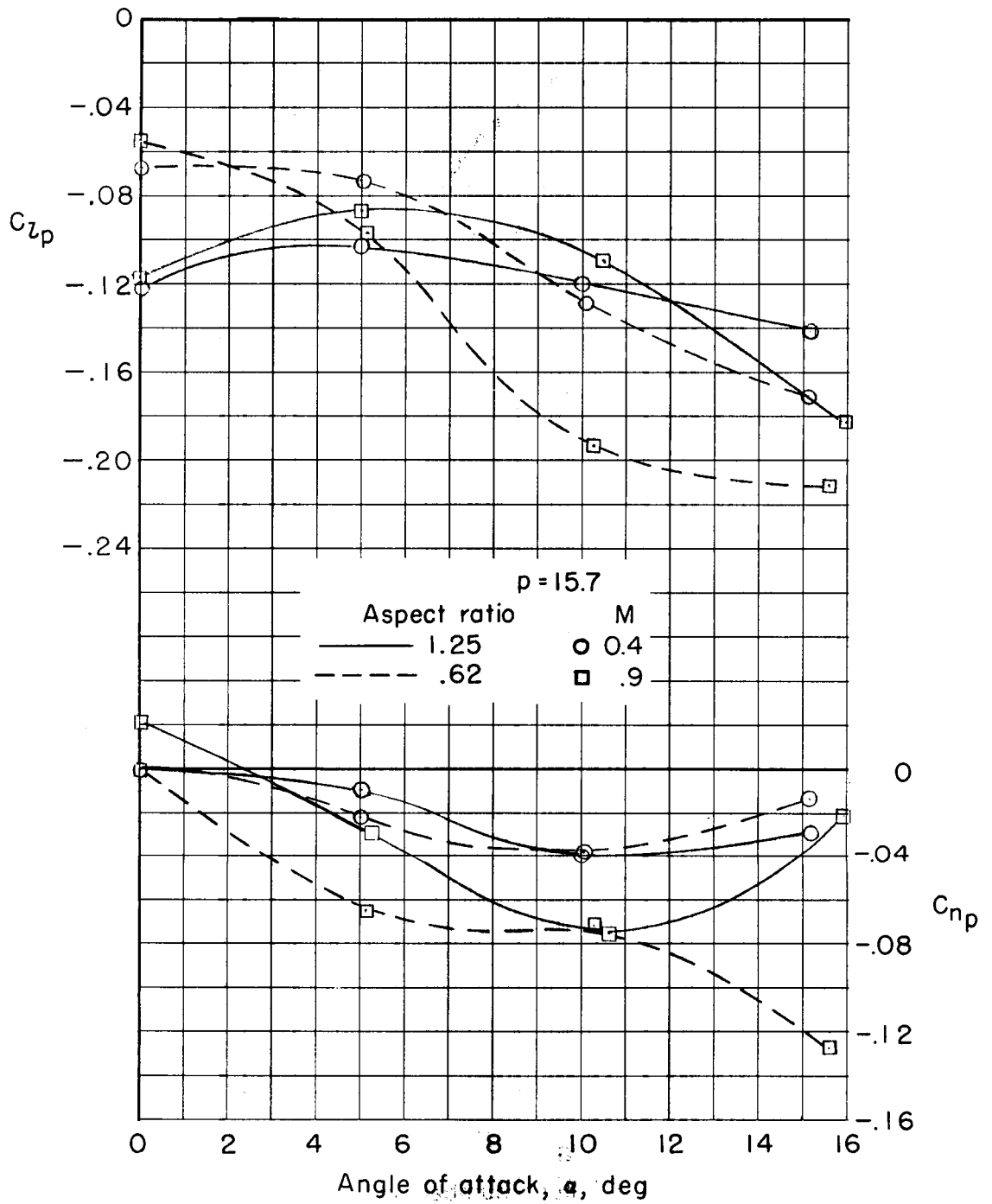

(a) p = 15.7 radians/sec.

Figure 13.- Effect of aspect ratio on C_{l_p} and C_{n_p}. Stability axis.

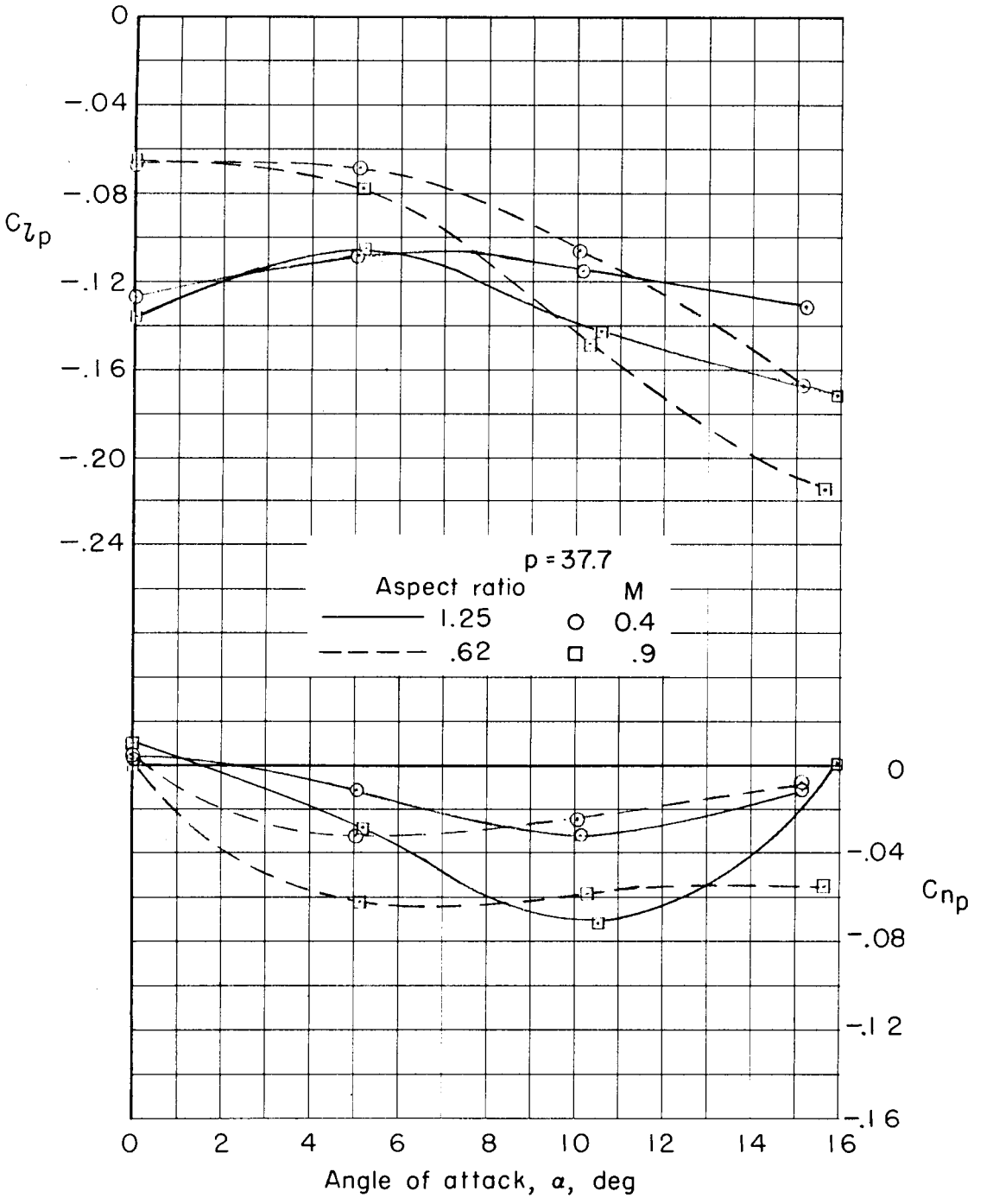

(b) p = 37.7 radians/sec.

Figure 13.- Concluded.

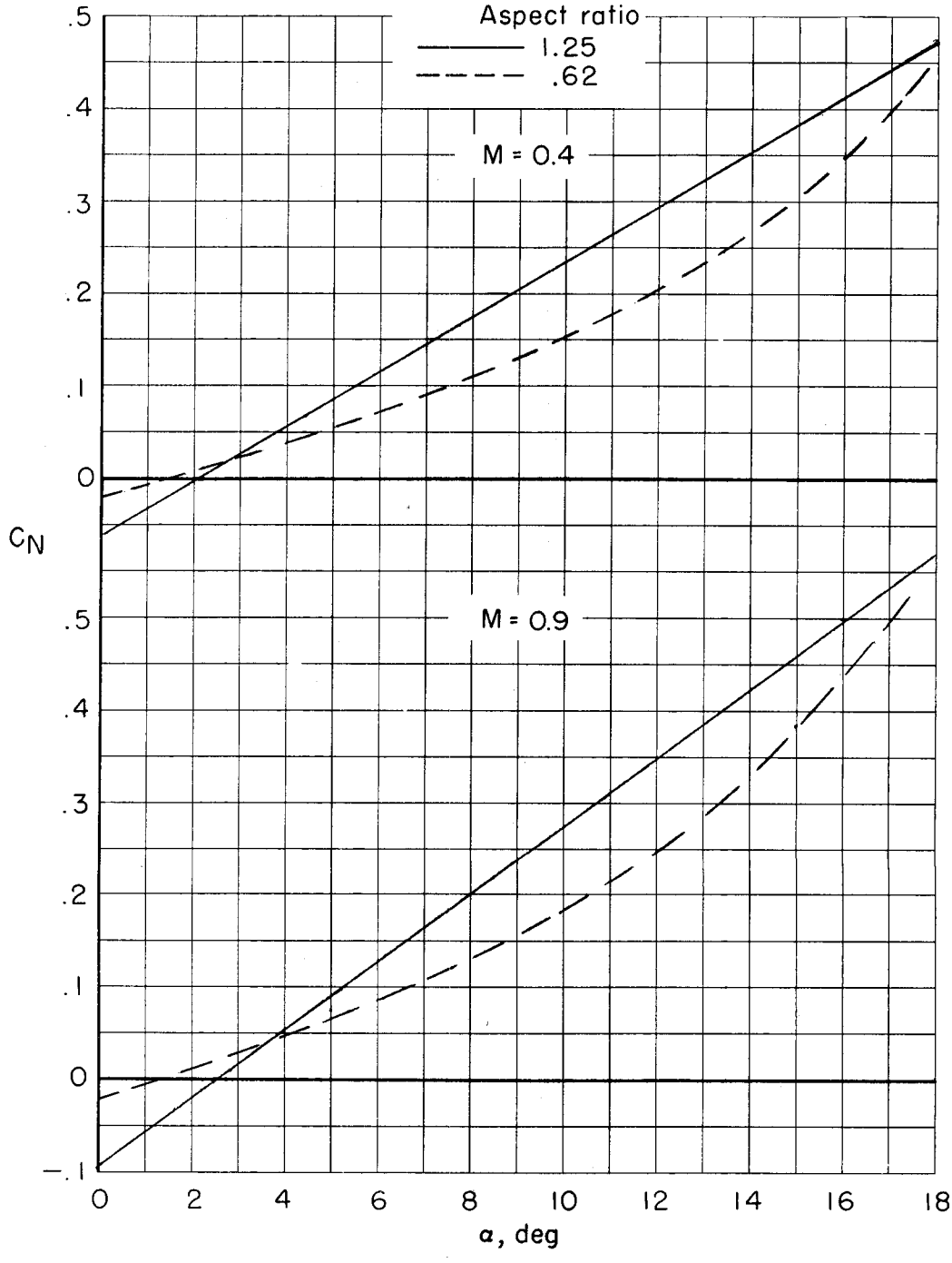

Figure 14.- Variation of normal-force coefficient with angle of attack for the narrow and the wide models.

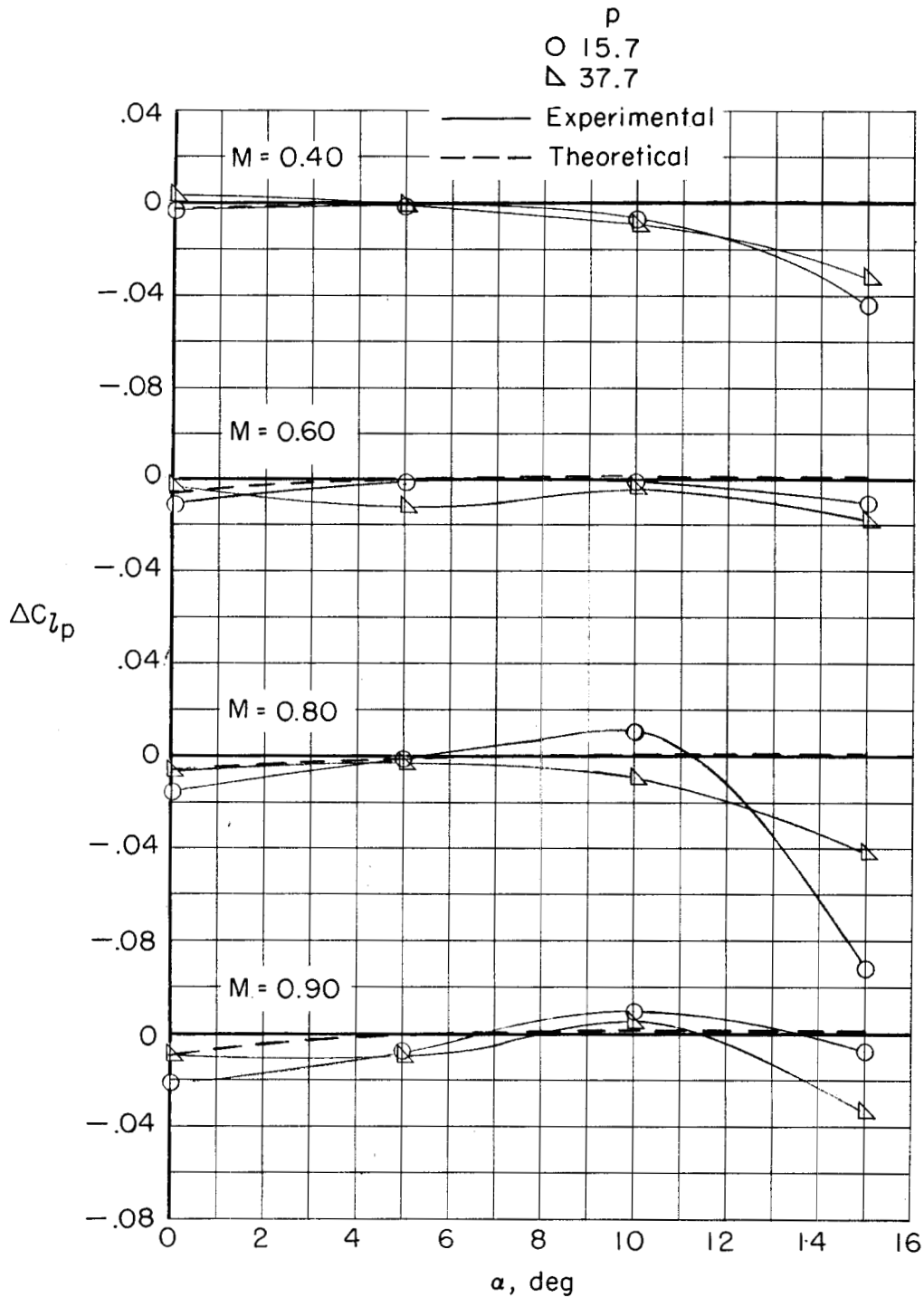

Figure 15.- Increment of C_{l_p} due to a vertical tail on the model with an aspect ratio of 0.62. Stability axis.

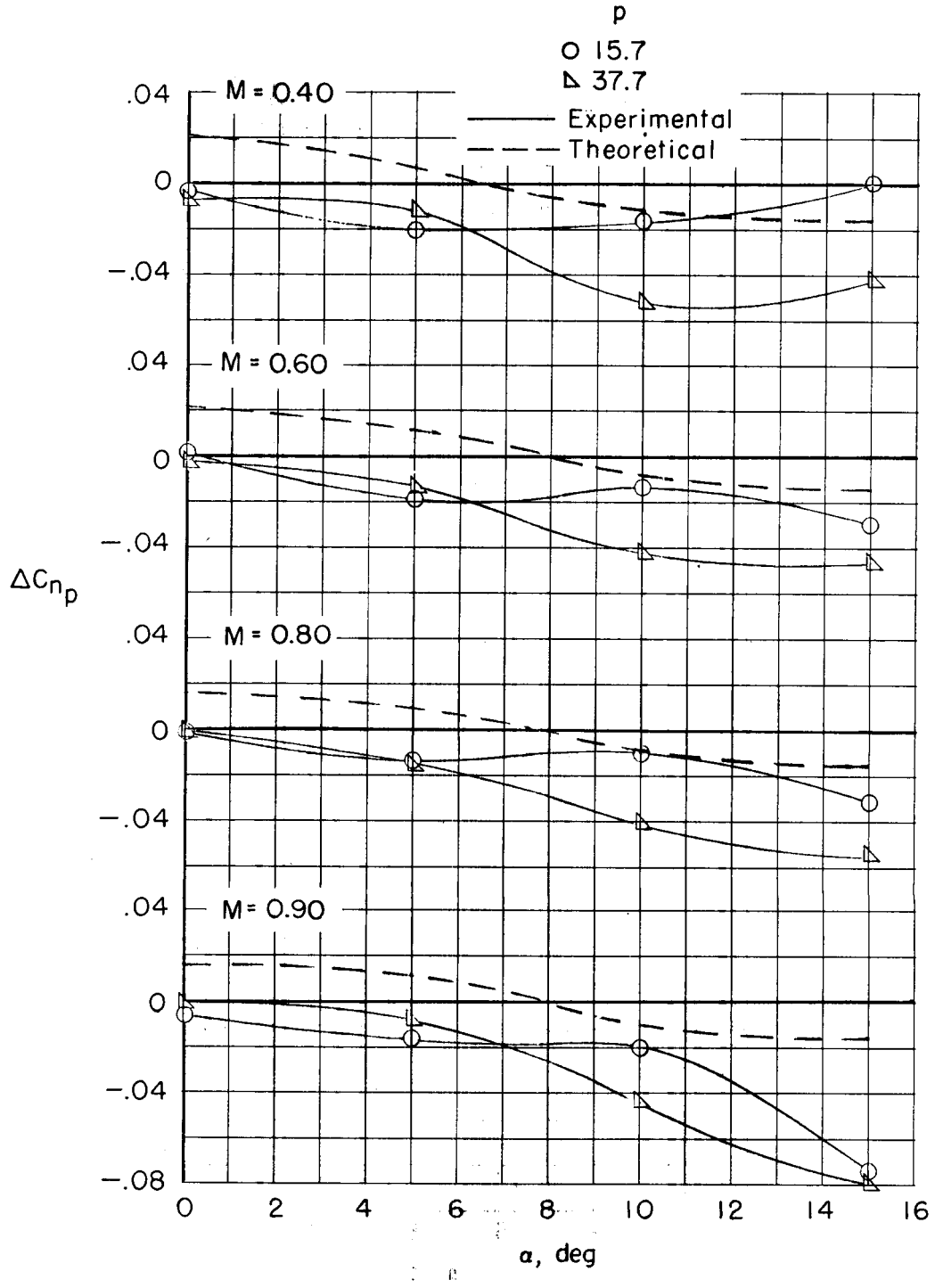

Figure 16.- Increment of C_{n_p} due to a vertical tail on model with an aspect ratio of 0.62. Stability axis.